nature communications

Article

https://doi.org/10.1038/s41467-024-54817-7

NET formation-mediated in situ protein delivery to the inflamed central nervous system

Received: 8 April 2024

Accepted: 18 November 2024

Published online: 30 December 2024

Check for updates

Yina Wu[1,5], Jinwon Park[1,5], Quoc-Viet Le[2], Junho Byun[3], Jaehyun Choi[1], Enzhen Xu[1], Jaiwoo Lee[1,4] ✉ & Yu-Kyoung Oh[1] ✉

Delivering protein drugs to the central nervous system (CNS) is challenging due to the blood-brain and blood-spinal cord barrier. Here we show that neutrophils, which naturally migrate through these barriers to inflamed CNS sites and release neutrophil extracellular traps (NETs), can be leveraged for therapeutic delivery. Tannic acid nanoparticles tethered with anti-Ly6G antibody and interferon-β (aLy6G-IFNβ@TLP) are constructed for targeted neutrophil delivery. These nanoparticles protect interferon-β from reactive oxygen species and preferentially accumulate in neutrophils over other immune cells. Upon encountering inflammation, neutrophils release the nanoparticles during NET formation. In the female mouse model of experimental autoimmune encephalomyelitis, intravenous administration of aLy6G-IFNβ@TLP reduce disease progression and restore motor function. Although this study focuses on IFNβ and autoimmune encephalomyelitis, the concept of hitchhiking neutrophils for CNS delivery and employing NET formation for inflamed site-specific nanoparticle release can be further applied for delivery of other protein drugs in the treatment of neurodegenerative diseases.

The regulated transport of molecules to the central nervous system (CNS), comprising the brain and spinal cord, is governed by the blood-brain barrier (BBB) and blood-spinal cord barrier[1]. These semipermeable membrane structures play a crucial role in sequestering the CNS from potentially harmful molecules, maintaining homeostasis through diverse transporter systems, tight junctions, and adherens junctions, yet concurrently impeding the ingress of therapeutic agents into the CNS[2]. Moreover, drugs must penetrate into the CNS parenchyma regardless of the route of administration.

Considering these barriers as major challenges in CNS drug delivery, various strategies have been investigated to overcome these physiological obstacles. The disruption of barriers through physical stimulations, like focused ultrasound with microbubbles, electroacupuncture, and intra-arterial injection of hyperosmotic mannitol, has been proposed as a strategy for breaching the BBB[2–4]. However, these approaches have been shown to damage blood vessels, cause microhemorrhages in the brain, and repeated stimulation can lead to severe inflammation. Moreover, transient BBB opening can also cause non-selective transfer of blood components into the CNS, leading to CNS toxicity[5].

Invasive strategies such as intrathecal drug delivery and direct brain injection can also achieve drug delivery into the CNS without passing through the BBB[6,7]. Intrathecal administration of the antisense oligonucleotide nusinersen has been approved to treat spinal muscular atrophy[8]. Direct CNS delivery of nusinersen has been shown to improve motor function rather than just slowing down disease progression. However, these invasive technologies have the potential for CNS exposure and subsequent tissue damage, limiting their long-term use. Therefore, alternative non-invasive strategies to penetrate the BBB and blood-spinal cord barrier for

[1]College of Pharmacy and Research Institute of Pharmaceutical Sciences, Seoul National University, Seoul, Republic of Korea. [2]Faculty of Pharmacy, Ton Duc Thang University, Ho Chi Minh City, Vietnam. [3]College of Pharmacy, Sookmyung Women's University, Seoul, Republic of Korea. [4]College of Pharmacy, Korea University, Sejong, Republic of Korea. [5]These authors contributed equally: Yina Wu, Jinwon Park. ✉e-mail: ljw1112@korea.ac.kr; ohyk@snu.ac.kr

selective CNS drug delivery without tissue damage are required to be developed.

Neutrophils (NEs) serve as the first responders to inflammation and migrate to inflammatory sites via chemotaxis[9]. Upon activation, NEs release neutrophil extracellular traps (NETs), which are extracellular fibers with web-like structures composed of DNA and granule proteins, via an active cell death pathway termed NETosis[10]. Due to these characteristics, NEs can be considered as an adequate cell-based drug delivery system for inflammatory disease therapy. Specifically, NEs can traverse barriers and migrate into the inflamed CNS due to released inflammatory factors in neurological disorders[11]. Delivery systems based on NEs, involving the loading of drugs into native NEs ex vivo and infusing drug-loaded NEs back into disease models, have shown therapeutic potential in the preclinical treatment of diseases such as glioblastoma and bone disorders[11,12].

In this study, we hypothesized that protein drug delivery to the CNS can be achieved by using the biological barrier-passing capability of NEs, and the NET formation at the inflamed sites. To test the hypothesis, we designed a tannic acid nanoparticle functionalized with anti-Ly6G antibody and IFNβ (aLy6G-IFNβ@TLP) for hitchhiking with circulating NEs to deliver IFNβ-tethered nanoparticles into the CNS (Fig. 1). Here, we report a safe and precise non-invasive strategy for NET formation-mediated in situ protein drug delivery to the inflamed CNS for the treatment of neurological disorders.

Results

Preparation and characterization of nanoparticles

The aLy6G-IFNβ@TLP were prepared by conjugating IFNβ and aLy6G with TLP using thiol-maleimide reaction (Fig. 2a). This formulation consisted of carbon (C), oxygen (O), and phosphorous (P) with a spherical morphology (Fig. 2b). The aLy6G-IFNβ@TLP were 205.1 ± 11.03 nm in size and had a surface charge of −38.45 ± 1.68 mV (Fig. 2c,d). The conjugation of aLy6G to the surfaces of nanoparticles was confirmed by sodium dodecyl sulfate-polyacrylamide gel electrophoresis (SDS-PAGE) and flow cytometry (Fig. 2e,f). The aLy6G-IFNβ@TLP contained 19.0 ± 0.48 μg tannic acid, 6425.07 ± 648.23 U IFNβ, and 48.17 ± 0.56 μg aLy6G per mg nanoparticles (Supplementary Fig. 1).

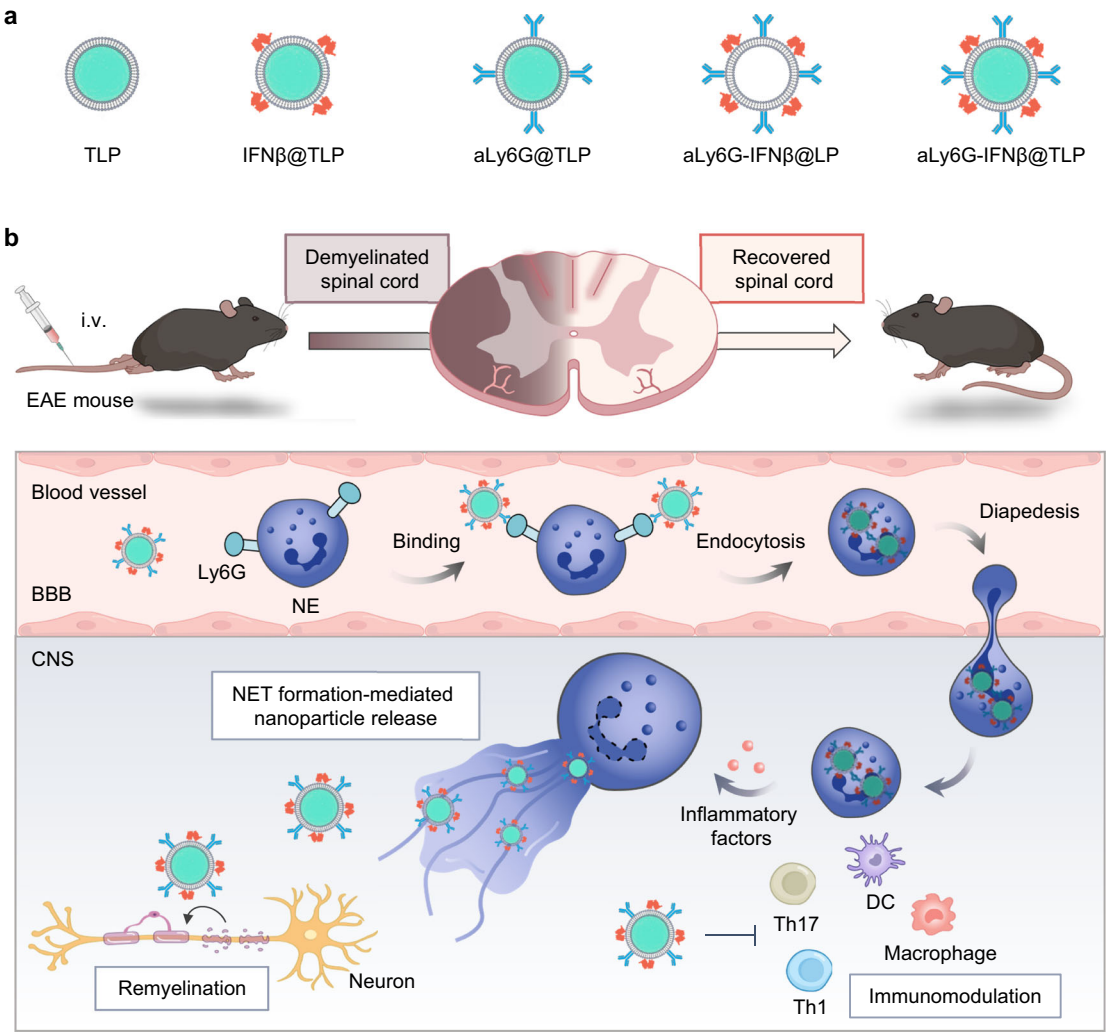

Fig. 1 | Schematic illustration of NET formation-mediated cytokine delivery to the inflamed CNS. a Schematic illustration of various nanoparticles tested in this study. TLP is a tannic acid core nanoparticle coated with lipid membranes. TLP was modified with IFNβ, anti-Ly6G antibody, or with both IFNβ and anti-Ly6G antibody, resulting in IFNβ@TLP, aLy6G@TLP, and aLy6G-IFNβ@TLP, respectively. For comparison, lipid nanoparticles modified with IFNβ and anti-Ly6G antibody, termed aLy6G-IFNβ@LP, were constructed. **b** Schematic illustration of NET formation-mediated IFNβ delivery to the inflamed CNS for ameliorating the experimental autoimmune encephalomyelitis (EAE). By binding to Ly6G on NEs, aLy6G-IFNβ@TLP can cross the BBB via NE hitchhiking and reach to the inflamed CNS. Upon activation by inflammatory factors, NET formation results in the release of aLy6G-IFNβ@TLP. Consequently, aLy6G-IFNβ@TLP can deliver IFNβ into the inflamed CNS, generating remyelination and immunomodulation effects against EAE.

https://doi.org/10.1038/s41467-024-54817-7

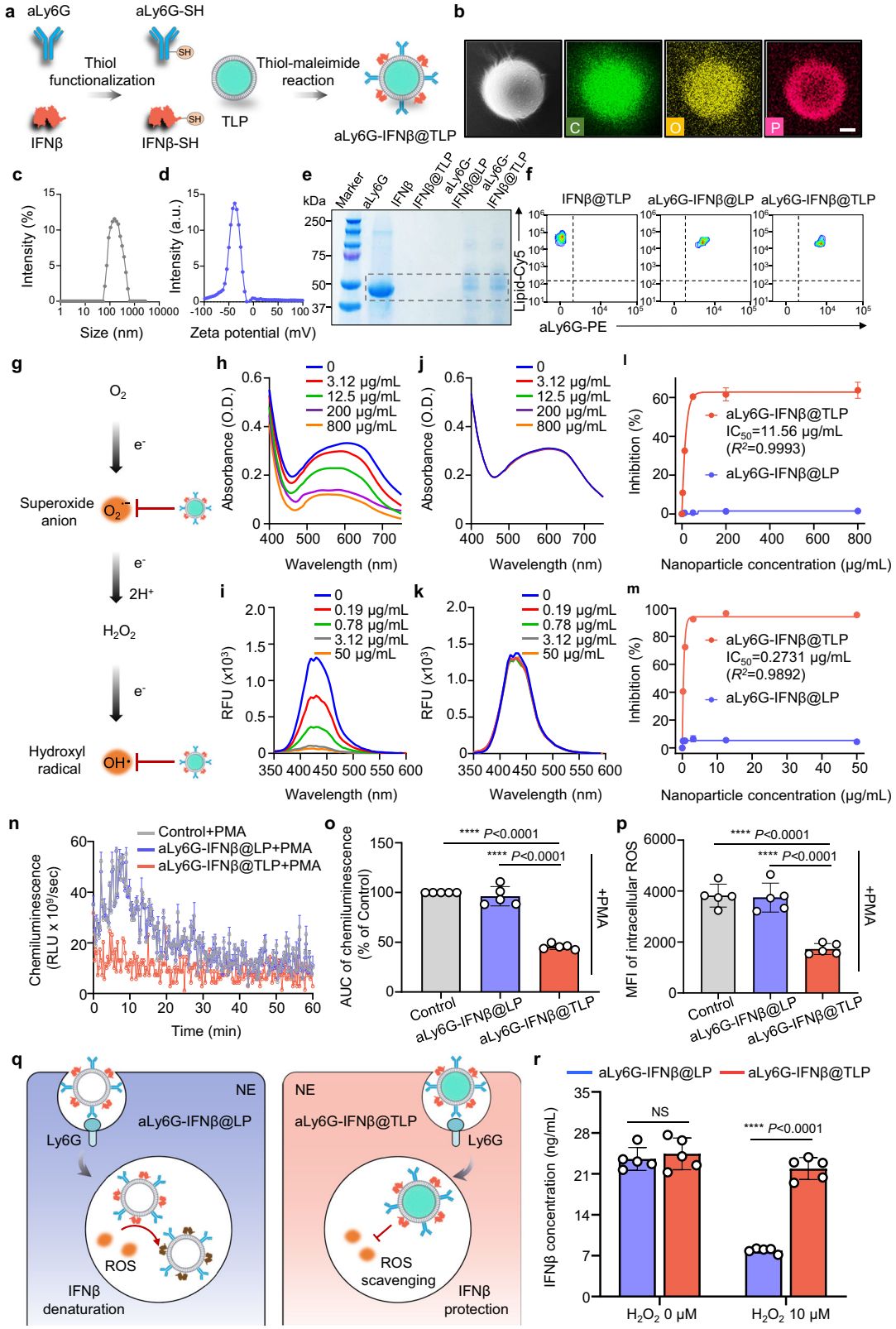

The aLy6G-IFNβ@TLP showed the ability to scavenge reactive oxygen species (ROS) such as superoxide anion and hydroxyl radical (Fig. 2g). The superoxide anion and hydroxyl radical scavenging activity of aLy6G-IFNβ@TLP was concentration-dependent (Fig. 2h,i). On the contrary, the NE hitchhiking formulation without tannic acid (aLy6G-IFNβ@LP) showed no ability to eliminate ROS (Fig. 2j,k). Half maximal inhibitory concentration (IC_{50}) of aLy6G-IFNβ@TLP was calculated to be 11.56 μg/mL for superoxide anion scavenging (Fig. 2l) and 0.2731 μg/mL for hydroxyl radical scavenging (Fig. 2m), respectively.

To explore the various effects of aLy6G-IFNβ@TLP in vitro, NEs were isolated from bone marrow and gated as Gr-1$^+$CD11b$^+$ cells for further analysis (Supplementary Fig. 2). The cell viability of NEs was not affected by the presence of nanoparticles, showing no significant

Fig. 2 | Physicochemical and biological characteristics of nanoparticles. **a** Preparation scheme of aLy6G-IFNβ@TLP. **b** EDS-SEM images of aLy6G-IFNβ@TLP. Scale bar: 50 nm. The experiment was repeated twice independently with similar results and the representative data is shown. **c** Particle size distribution of aLy6G-IFNβ@TLP measured by dynamic light scattering. **d** Zeta potential of aLy6G-IFNβ@TLP. **e** SDS-PAGE analysis of aLy6G conjugation on various formulations. The experiment was repeated twice independently with similar results and the representative data is shown. **f** Flow cytometry analysis of aLy6G conjugation on various formulations. **g** ROS scavenging effect of aLy6G-IFNβ@TLP. **h** Dose-dependent superoxide anion scavenging activity of aLy6G-IFNβ@TLP, assessed by nitro blue tetrazolium assay. **i** Dose-dependent hydroxyl radical scavenging activity of aLy6G-IFNβ@TLP, evaluated by terephthalic acid assay. **j**, **k** Dose-dependent superoxide anion scavenging activity (**j**) and hydroxyl radical scavenging activity (**k**) of aLy6G-IFNβ@LP. **l** Quantification of IC_{50} for superoxide anion scavenging activity ($n = 3$ independent samples per group). **m** Quantification of IC_{50} for hydroxyl radical scavenging activity ($n = 3$ independent samples per group). **n** Evaluation of intracellular ROS generation of NEs after PMA stimulation and nanoparticle treatment by chemiluminescence assay ($n = 5$ biologically independent samples per group). **o** Area under the curve (AUC) of chemiluminescence ($n = 5$ biologically independent samples per group). Statistical significance was analyzed using one-way ANOVA with Tukey's multiple comparisons test. $P_{aLy6G\text{-}IFN\beta@TLP\text{-}Control} < 0.0001$, $P_{aLy6G\text{-}IFN\beta@TLP\text{-}aLy6G\text{-}IFN\beta@LP} < 0.0001$. **p** Mean fluorescence intensity (MFI) of intracellular ROS upon PMA stimulation evaluated by flow cytometry ($n = 5$ biologically independent samples per group). Statistical significance was analyzed using one-way ANOVA with Tukey's multiple comparisons test. $P_{aLy6G\text{-}IFN\beta@TLP\text{-}Control} < 0.0001$, $P_{aLy6G\text{-}IFN\beta@TLP\text{-}aLy6G\text{-}IFN\beta@LP} < 0.0001$. **q** Underlying mechanism of denaturation and protection of IFNβ in aLy6G-IFNβ@LP and aLy6G-IFNβ@TLP under ROS-rich environment. **r** Determination of IFNβ stability released from aLy6G-IFNβ@LP and aLy6G-IFNβ@TLP in the absence and presence of H_2O_2 ($n = 5$ independent samples per group). Statistical significance was analyzed using unpaired two-sided *t*-test. At H_2O_2 0 μM, NS, not significant. At H_2O_2 10 μM, $P_{aLy6G\text{-}IFN\beta@TLP\text{-}aLy6G\text{-}IFN\beta@LP} < 0.0001$. Data are presented as mean ± s.d. Source data are provided as a Source Data file. RFU, relative fluorescence unit. a.u., arbitrary units.

cellular toxicity compared with control group (Supplementary Fig. 3). Depending on nanoparticles, ROS elimination capability differed. The aLy6G-IFNβ@TLP eliminated intracellular ROS in NEs upon phorbol 12-myristate 13-acetate (PMA) activation, whereas aLy6G-IFNβ@LP could not (Fig. 2n-p). The stability of IFNβ differed between nanoparticles with and without tannic acid (Fig. 2q). The stability of IFNβ at aLy6G-IFNβ@LP group significantly decreased by ROS. In contrast, IFNβ conjugated with aLy6G@TLP maintained stability in ROS-rich condition (Fig. 2r).

Specificity of NE binding

Functionalizing the nanoparticles with aLy6G enhanced their binding ability to NEs. To assess the NE-mediated CNS delivery of drug-loaded nanoparticles, an in vitro BBB model using a transwell system was employed. The BBB cell model was established by seeding bEnd.3, endothelial cells, on the apical side of transwell inserts and incubating them for 7 days until a very compact monolayer formed (Fig. 3a). Modification of nanoparticles with aLy6G significantly enhanced the binding ability of NEs compared with IFNβ@TLP (Fig. 3b). To investigate whether aLy6G modification allowed specific binding of nanoparticles to NEs, we examined the binding ability of nanoparticles on T cells, and antigen-presenting cells (APCs) such as B cells, dendritic cells (DCs), and macrophages (Supplementary Fig. 4). Regardless of T cells and APCs, there was no significant difference in the binding or uptake between nanoparticles with or without aLy6G modification.

To investigate whether aLy6G-IFNβ@TLP were internalized or just bound to the surface of NEs, we labeled nanoparticles with Fe^{3+} by chelating tannic acid with Fe^{3+} to form dark-colored nanoparticles and observed them using TEM. We observed that aLy6G-IFNβ@TLP were internalized by NEs (Fig. 3c). The internalization of aLy6G-IFNβ@TLP was most highly inhibited by chlorpromazine and chloroquine compared to methyl-β-cyclodextrin, amiloride, and cytochalasin D (Supplementary Fig. 5). Subsequently, we assessed the NE migration across the endothelial monolayer after nanoparticle treatment in the presence of formylmethionyl-leucyl-phenylalanine (fMLP), a chemotactic peptide (Fig. 3d). The aLy6G-IFNβ@TLP did not affect the migration capability of NEs under chemotaxis (Fig. 3e). Cyanine-5 (Cy5)-labeled IFNβ@TLP showed little transportation in the presence of fMLP. In contrast, Cy5-labeled aLy6G-IFNβ@TLP bound with NEs passed across the monolayer (Fig. 3f).

NET formation-mediated release of nanoparticles

The modification of nanoparticles with aLy6G influenced the release of nanoparticles via NET formation. When nanoparticle-treated NEs were stimulated with PMA to induce NET formation, little signal of IFNβ@TLP was observed in the NET (Fig. 3g). Unlike IFNβ@TLP, both aLy6G-IFNβ@TLP and aLy6G-IFNβ@LP showed strong signals in the NET (Fig. 3g and Supplementary Fig. 6a). Particularly, the signals were colocalized with myeloperoxidase (MPO), an important component of NET (Fig. 3h and Supplementary Fig. 6b). The Pearson's correlation coefficient between nanoparticles and MPO in the aLy6G-IFNβ@TLP group was significantly higher compared to the IFNβ@TLP group, indicating the release of aLy6G-IFNβ@TLP during the process of NET formation (Fig. 3i).

Upon PMA activation, NEs underwent significant morphological changes and released NET (Fig. 3j,k). Throughout this process, internalized aLy6G-IFNβ@TLP were released within 4 h upon PMA activation. The release of nanoparticles from NEs was also captured in real-time live cell-imaging (Fig. 3l and Supplementary Video 1). The video recording upon PMA activation showed that aLy6G-IFNβ@TLP were internalized by NEs initially and began to be released into the extracellular area 45 min after PMA treatment (Supplementary Video 1). The fluorescence signals of Hoechst and aLy6G-IFNβ@TLP were colocalized and began to separate 30 min post-treatment with PMA (Fig. 3m).

Once transported and released into the CNS, IFNβ should be released. To facilitate the release of IFNβ, nanoparticles were conjugated with IFNβ via thiol-maleimide reaction, forming a thioether linkage susceptible to deconjugation via a retro-Michael pathway[13]. The conjugated IFNβ can be replaced by serum albumin thiol, leading to the release of IFNβ (Fig. 3n). The IFNβ release profiles of aLy6G-IFNβ@TLP differed between PBS and fetal bovine serum (FBS) media. Compared to PBS media, FBS showed sustained time-dependent release of IFNβ. At 72 h time point, 22% of IFNβ was released in PBS, while 82% of IFNβ was released in FBS (Fig. 3o).

Inflamed CNS accumulation of nanoparticles

The modification of nanoparticles with aLy6G facilitated in situ hitchhiking with NEs and promoted the delivery of nanoparticles to the CNS. The CNS accumulation of nanoparticles in inflamed conditions was assessed in EAE mice. Intravenous injection of Cy5-labeled aLy6G-IFNβ@TLP exhibited significantly stronger fluorescence signals in both the brain and spinal cord compared to the IFNβ@TLP-administered group (Fig. 4a,b). Furthermore, aLy6G-IFNβ@TLP administration showed the highest signals in both brain and spinal cord at 6 h post-injection, which were 4.35- and 11.69-fold higher than those of IFNβ@TLP, respectively (Fig. 4c,d). The distribution of nanoparticles to peripheral organs varied depending on the nanoparticle type. IFNβ@TLP showed the highest accumulation in the liver at 1 h post-dose, followed by a decrease at 6 h post-dose (Supplementary Fig. 7a). In contrast, aLy6G-IFNβ@TLP exhibited peak distribution in the liver and lungs at 6 h post-administration, with a subsequent decline at 12 h post-dose (Supplementary Fig. 7b).

Next, we explored the cellular distribution of nanoparticles in different immune cells in the spinal cord. We identified NEs as CD11b-

https://doi.org/10.1038/s41467-024-54817-7

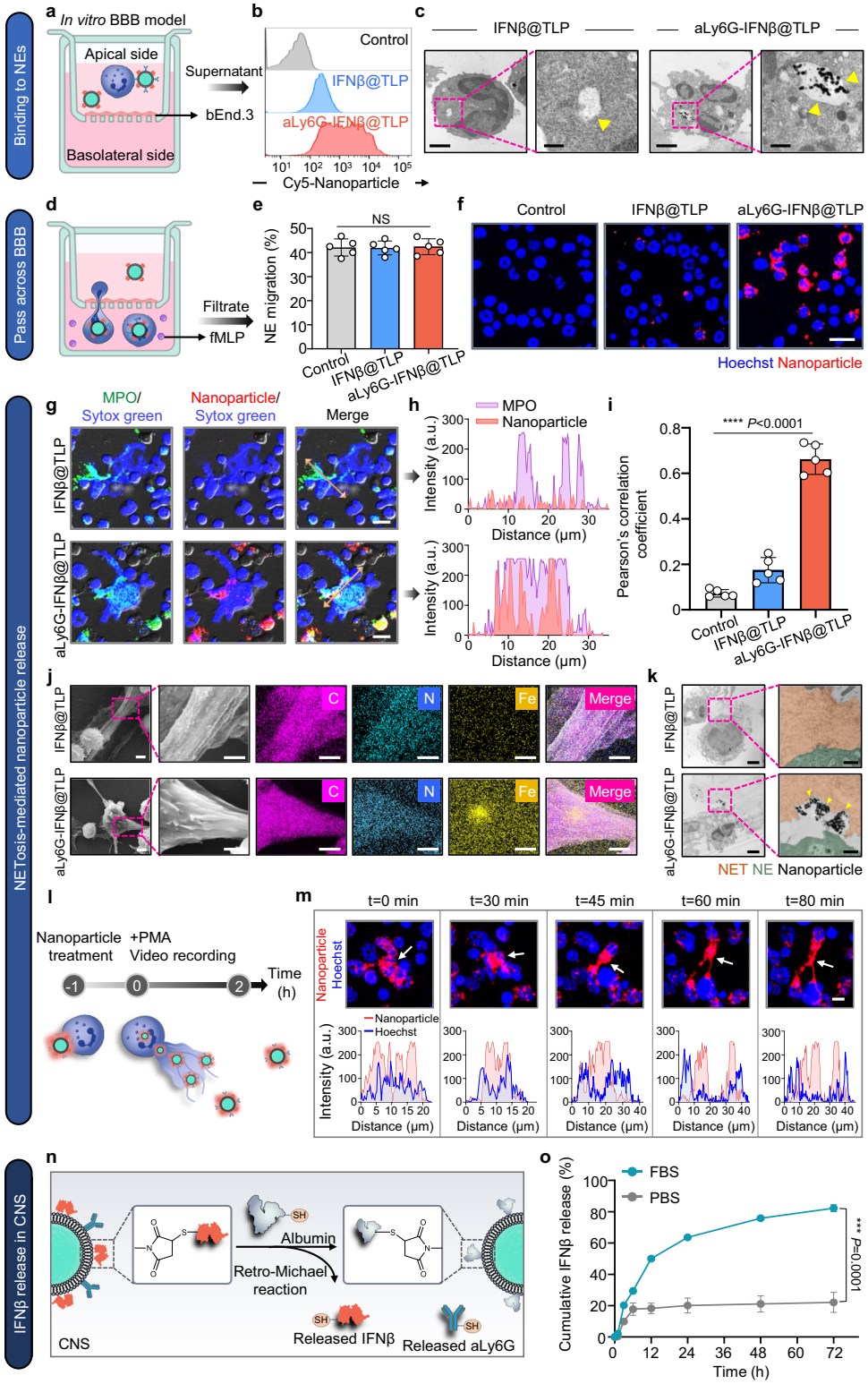

and Ly6G-positive cells among CD45-positive leukocytes (Fig. 4e). The MFI of aLy6G-IFNβ@TLP in NEs was 8.53-fold higher than that of IFNβ@TLP 6 h post-administration (Fig. 4f). Fluorescence imaging also revealed the colocalization of aLy6G-IFNβ@TLP with Ly6G-expressing NEs in the spinal cord (Fig. 4g,h). Additionally, we gated the most abundant immune cells that aggressively infiltrate the CNS during the progression of EAE which were T cells and APCs (Supplementary Fig. 8). The fluorescence signal of aLy6G-IFNβ@TLP colocalized with NEs, while little signal was detected in T cells and APCs populations. Little signal of IFNβ@TLP was observed in the immune cell populations (Fig. 4i,j). We then employed intravital microscopy to monitor real-time nanoparticle infiltration into the inflamed spinal cord (Fig. 4k). After establishing the EAE mice model, fluorescence-labeled nanoparticles and dextran were intravenously injected. The anterior spinal artery of the thoracic region was exposed, and nanoparticle infiltration was monitored. At 3 h post-administration, the signal of aLy6G-IFNβ@TLP was observed inside the anterior spinal artery, whereas no obvious signal of IFNβ@TLP was detected (Fig. 4l).

Fig. 3 | In vitro NE binding and NET formation-mediated release of nanoparticles. a Schematic illustration of the in vitro BBB model for assessing NE binding and penetration ability of aLy6G-IFNβ@TLP across the endothelial monolayer. **b** Evaluation of NE binding capability of different formulations using flow cytometry. **c** Visualization of internalization of Fe-labeled nanoparticles in NEs using TEM. Scale bar: 2 μm. Scale bar of expanded images: 0.5 μm. The experiment was repeated twice independently with similar results and the representative data is shown. **d** Schematic illustration of nanoparticle-bound NEs migration across the endothelial monolayer in the presence of fMLP. **e** Migration of NEs and nanoparticle-treated NEs across the endothelial monolayer in the presence of fMLP ($n = 5$ biologically independent samples per group). Statistical significance was analyzed using one-way ANOVA with Tukey's multiple comparisons test. NS, not significant. **f** Confocal images of nanoparticle-bound NEs in the filtrate. Scale bar: 20 μm. The experiment was repeated twice independently with similar results and the representative data is shown. **g** Confocal images of NET formation-mediated nanoparticle release after incubation with PMA for 4 h. Scale bar, 10 μm. The experiment was repeated twice independently with similar results and the representative data is shown. **h** Evaluation of colocalization of MPO with nanoparticles in the NET. **i** Pearson's correlation coefficient of MPO with nanoparticles in the NETs ($n = 5$ biologically independent samples per group). Statistical significance was analyzed using one-way ANOVA with Tukey's multiple comparisons test. $P_{aLy6G\text{-}IFN\beta@TLP\text{-}Control} < 0.0001$, $P_{aLy6G\text{-}IFN\beta@TLP\text{-}IFN\beta@TLP} < 0.0001$. **j** Visualization of Fe-labeled aLy6G-IFNβ@TLP release during the process of NET formation by EDS-SEM. Scale bar: 2 μm. Scale bar of expanded images: 1 μm. The experiment was repeated twice independently with similar results and the representative data is shown. **k** TEM images of NET formation-induced aLy6G-IFNβ@TLP release in the NET. Scale bar: 2 μm for left panels, 0.5 μm for right panels. The experiment was repeated twice independently with similar results and the representative data is shown. **l** Experimental design for monitoring the process of PMA-induced NET formation and nanoparticle release. **m** Release of aLy6G-IFNβ@TLP and their colocalization with Hoechst were observed over time. NEs nuclei were stained with Hoechst 33342, and aLy6G-IFNβ@TLP were labeled with Cy5. Scale bar: 5 μm. The experiment was repeated twice independently with similar results and the representative data is shown. **n** The underlying mechanism of IFNβ release in the inflamed CNS. **o** Cumulative IFNβ release from aLy6G-IFNβ@TLP in PBS or FBS solution ($n = 3$ independent samples per group). Statistical significance was analyzed using unpaired two-sided t-test. $P_{FBS\text{-}PBS} = 0.0001$. Data are presented as mean ± s.d. Source data are provided as a Source Data file.

Therapeutic efficacy of nanoparticles in the EAE mouse model

In situ NE hitchhiking enhanced the therapeutic efficacy of aLy6G-IFNβ@TLP in the EAE mouse model. Prior to evaluate the therapeutic efficacy of aLy6G-IFNβ@TLP, we tested maximum tolerated dose of aLy6G@TLP, where TLP is modified with aLy6G alone for determining the optimal in vivo regimen for EAE treatment. aLy6G@TLP with different doses were intravenously injected to the healthy C57BL/6 mice and this administration was repeated three times every three days (Supplementary Fig. 9a). A dose of 40 mg per kg of aLy6G@TLP, showed consistent body weight increase, and was chosen as a dose for repeated administration in this study (Supplementary Fig. 9b).

Previous studies have been reported an increased number of infiltrated NEs in the spinal cord from day 12 post-immunization until day 21[14,15]. To determine the location of NET formation, various organs were stained with citrullinated histone H3, a specific marker for NETs. We found that NET formation began as early as day 12 in the brain and spinal cord, but was scarcely observed in peripheral organs such as the spleen, liver, and lungs (Supplementary Fig. 10). To determine the optimal regimen for this treatment, we analyzed changes in clinical scores following aLy6G-IFNβ@TLP treatment. The therapy exhibited a dose-dependent effect on EAE, with a significant therapeutic response observed at a dose of 5000 U of IFNβ administered three times, every three days, starting 12 days after EAE immunization (Supplementary Fig. 11a,b). The clinical scores also varied depending on the timing of the initial injection, suggesting that NE hitchhiking enhanced the therapeutic effect (Supplementary Fig. 11c,d). Additionally, the effectiveness of the treatment was influenced by the dosing frequency, with three doses identified as the optimal regimen (Supplementary Fig. 11e,f).

Consequently, various nanoparticles were intravenously administered 12 days after EAE immunization, and this treatment regimen was repeated three times every three days (Fig. 5a). Treatment with aLy6G-IFNβ@TLP resulted in slightly body weight loss at the peak stage, which recovered by the end of the study, in contrast to IFNβ@TLP and aLy6G-IFNβ@LP, which leading to significant body weight loss at both peak and recovery stages (Fig. 5b). Furthermore, aLy6G-IFNβ@TLP treatment effectively ameliorated clinical symptoms, with the maximal clinical score reaching 1.4 ± 0.42 and decreased to 0.5 ± 0.61 by the end of study (Fig. 5c). In contrast, mice treated with IFNβ@TLP and aLy6G-IFNβ@LP exhibited typical motor symptoms of the disease.

Various cytokine production levels in splenocytes were assessed in mice treated with different nanoparticle formulations. Splenocytes were stimulated with $MOG_{35\text{-}55}$ at the end of the study. The production of IL-17, TNF-α, IFN-γ, and IL-6 were significantly lower in the group treated with aLy6G-IFNβ@TLP compared to the groups treated with IFNβ@TLP and aLy6G-IFNβ@LP (Fig. 5d–g). The levels of IFN-γ, IL-17, and IL-6 in the blood were significantly reduced in mice treated with aLy6G-IFNβ@TLP (Fig. 5h,i and Supplementary Fig. 12).

The effect of nanoparticle treatment on neuroglia was tested on astrocytes and microglia. In aLy6G-IFNβ@TLP-treated mice, the expression of pro-inflammatory genes (*Il6, Il23a*, and *Ccl20*) (Supplementary Fig. 13b) and glial fibrillary acidic protein (GFAP) was downregulated in astrocytes compared to untreated EAE mice (Supplementary Fig. 13c,d). Additionally, the expression of markers associated with costimulatory molecules and phagocytosis (CD40, CD86, and CD68) (Supplementary Fig. 14b,c) and the expression of ionized calcium-binding adapter molecule 1 (Iba1) were reduced in microglia from aLy6G-IFNβ@TLP-treated mice (Supplementary Fig. 14d,e). These findings suggest that aLy6G-IFNβ@TLP treatment can modulate the activation of astrocytes and microglia under pathogenic CNS conditions.

Gene expression profiles

The administration of aLy6G-IFNβ@TLP influenced the expression levels of various genes associated with the progression of EAE in the spinal cord (Fig. 5j). Compared with PBS treatment, aLy6G-IFNβ@TLP increased the expression of myelin-associated proteins such as PLP1 and MBP, as well as the expression of antioxidant enzyme such as GPX1. The group treated with aLy6G-IFNβ@TLP showed decreased expression of leukocyte chemokines such as CCL3 and CXCL11, and chemokine receptors such as CXCR3 and CCR5. Moreover, aLy6G-IFNβ@TLP treatment decreased the expression of pro-inflammatory cytokine such as IL-6, as well as transcription factors such as HIF1A and JUN.

Immune modulation effect

To evaluate immune modulation and the restoration of the inflamed CNS in EAE, we assessed the populations of Th1, Th17, and total amounts of infiltrating immune cells in the spinal cord. The population of $CD4^+$ T cells producing IFN-γ was downregulated in the aLy6G-IFNβ@TLP treated mice (Fig. 6a,b). Treatment with aLy6G-IFNβ@TLP also resulted in a decreased IL-17A-expressing $CD4^+$ T cell population compared to IFNβ@TLP and aLy6G-IFNβ@LP (Fig. 6c,d). The total numbers of helper T cells ($CD45^+CD3^+CD4^+$) (Fig. 6e) and cytotoxic T cells ($CD45^+CD3^+CD8^+$) (Fig. 6f) in aLy6G-IFNβ@TLP treated mice were reduced. Furthermore, we observed that aLy6G-IFNβ@TLP therapy resulted in lower numbers of DCs ($CD45^+CD11c^+MHCII^+$) (Fig. 6g), and macrophages ($CD45^+CD11b^+F4/80^+$) (Fig. 6h), in the

https://doi.org/10.1038/s41467-024-54817-7

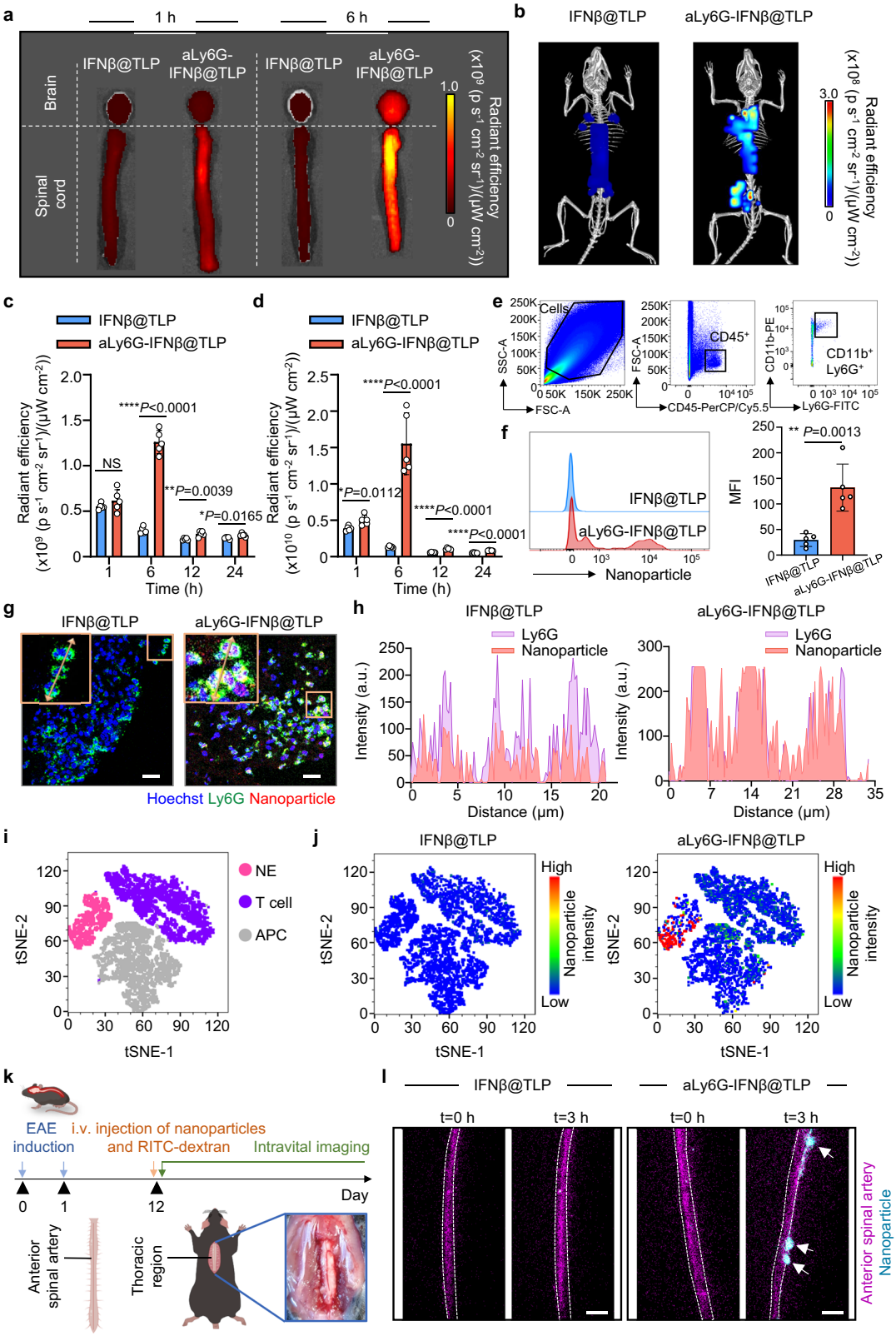

spinal cord, all of which play a predominant role in the progression of EAE.

Various histological analyses were conducted, revealing that aLy6G-IFNβ@TLP administration prevented the infiltration of CD45-expressing leukocytes into the spinal cord. In contrast, IFNβ@TLP and aLy6G-IFNβ@LP groups showed increased leukocytes infiltration (Fig. 6i,j). Demyelination of the spinal cord in aLy6G-IFNβ@TLP group was significantly reduced compared with IFNβ@TLP and aLy6G-IFNβ@LP (Fig. 6k,l).

Safety of nanoparticles

To assess the safety of the aLy6G-IFNβ@TLP, various biochemical parameters of blood were examined at the end of the in vivo experiments (Supplementary Fig. 15). Treatment of mice with aLy6G-

Fig. 4 | Distribution of nanoparticles to the inflamed CNS. a Ex vivo fluorescence imaging of brain and spinal cord in EAE mice following intravenous administration of IFNβ@TLP and aLy6G-IFNβ@TLP over time. **b** Whole-body molecular imaging of EAE mice at 6 h post-injection of IFNβ@TLP and aLy6G-IFNβ@TLP. Quantification of nanoparticle fluorescence in the brain (**c**) and spinal cord (**d**) of EAE mice after intravenous injection of different formulations over time ($n = 5$ biologically independent samples per group). Statistical significance was analyzed using unpaired two-sided *t*-test. For brain samples: 1 h, NS, not significant; 6 h, $P_{aLy6G\text{-}IFN\beta@TLP\text{-}IFN\beta@TLP} < 0.0001$; 12 h, $P_{aLy6G\text{-}IFN\beta@TLP\text{-}IFN\beta@TLP} = 0.0039$; 24 h, $P_{aLy6G\text{-}IFN\beta@TLP\text{-}IFN\beta@TLP} = 0.0165$. For spinal cord samples: 1 h, $P_{aLy6G\text{-}IFN\beta@TLP\text{-}IFN\beta@TLP} = 0.0112$; 6 h, $P_{aLy6G\text{-}IFN\beta@TLP\text{-}IFN\beta@TLP} < 0.0001$; 12 h, $P_{aLy6G\text{-}IFN\beta@TLP\text{-}IFN\beta@TLP} < 0.0001$; 24 h, $P_{aLy6G\text{-}IFN\beta@TLP\text{-}IFN\beta@TLP} < 0.0001$. **e** Gating strategy for NEs in the spinal cord, stained with PerCP/Cy5.5-conjugated CD45, FITC-conjugated Ly6G, and PE-conjugated CD11b antibodies. **f** Representative flow cytometry histogram (left) and quantification (right) of MFI of nanoparticles taken up by NEs in the spinal cord 6 h post-administration ($n = 5$ biologically independent samples per group). Statistical significance was analyzed using unpaired two-sided *t*-test. $P_{aLy6G\text{-}IFN\beta@TLP\text{-}IFN\beta@TLP} = 0.0013$. **g** Fluorescence images of the spinal cord after intravenous injection of nanoparticles for 6 h. Scale bar: 20 μm. The experiment was repeated twice independently with similar results and the representative data is shown. **h** Colocalization analysis of Ly6G-expressing cells and nanoparticles in the spinal cord. **i** t-SNE plot of single cells, color-coded according to the identified cell types. **j** t-SNE plots of nanoparticles taken up by T cells, APC, and NEs in the spinal cord, color-coded according to nanoparticle fluorescence intensity. **k** Experimental schedule for intravital imaging of spinal cord-infiltrated nanoparticles in EAE mice. **l** Intravital microscopy images of aLy6G-IFNβ@TLP-bound NEs migration into the spinal cord. Scale bar: 50 μm. The experiment was repeated twice independently with similar results and the representative data is shown. Data are presented as mean ± s.d. Source data are provided as a Source Data file.

IFNβ@TLP did not lead to significant changes in parameters related to liver functions, such as ALT, AST, and ALP, and kidney functions, including BUN and creatinine, compared with treatment with PBS. Additionally, the total protein value in the aLy6G-IFNβ@TLP group showed no difference compared to that in the PBS group.

Discussion

In this study, we demonstrated that aLy6G-IFNβ@TLP could be preferentially taken up by NEs and distribute to the inflamed brain via NEs. The functionalization of nanoparticles with aLy6G attributed to the specific uptake of nanoparticles by NEs. The release of nanoparticles by NET formation, and liberation of IFNβ showed the improvement of signs of CNS inflammation. Moreover, the use of tannic acid as core elements in nanoparticles contributed to the scavenging of ROS.

In this study, we selected IFNβ for delivery using nanoparticles. IFNβ, belonging to the interferon family, is a key treatment for multiple sclerosis (MS), particularly for relapsing-remitting MS in clinical settings. However, approximately 30% of patients do not respond to this therapy, and one contributing factor is the developing of high levels of neutralizing antibodies to IFNβ after systemic administration. Additionally, IFNβ therapy is currently available only in injectable forms, administered subcutaneously or intramuscularly, leading to severe skin reactions at the injection site, including irritation and necrosis[16]. It is noteworthy that intrathecal administration of IFNβ, through serial lumbar punctures in MS patients, has demonstrated a reduction in MS exacerbations[17,18]. This effect may be attributed to the direct immune modulation in the CNS and the enhancement of nerve growth factor production by IFNβ[19–21].

The use of tannic acid has been attributed to the stability of IFNβ in in vivo conditions. NEs have been reported to rapidly generate large amounts of ROS under inflammatory conditions. The exposure of IFNβ to ROS can lead to the denaturation of IFNβ inside the NEs before it can exert its therapeutic efficacy. To ensure the safe and effective delivery of IFNβ into the CNS, we employed tannic acid, a potent natural material capable of eliminating ROS, for ROS scavenging in NEs. We showed that IFNβ conjugated with aLy6G@LP denatured quickly in an H_2O_2 solution, whereas it could be effectively protected in the aLy6G@TLP formulation (Fig. 2p). The protection of IFNβ by the aLy6G@TLP platform correlated with the therapeutic efficacy in the EAE model, whereas aLy6G-IFNβ@LP treatment showed no significant reduction in exacerbations during the treatment period (Fig. 5).

We used NEs for carrying nanoparticles, and employed natural NET formation for release of nanoparticles to the inflamed CNS. The administration of ex vivo engineered NEs is challenging due to the properties of NEs. NEs have a short half-life, less than 1 day in circulation, which means there is small experimental time window to engineer NEs ex vivo[22]. Additionally, NEs cannot proliferate and be expanded ex vivo, limiting the available quantities of NEs. Moreover, NEs are highly responsive to a wide range of stimuli, leading to degranulation and the formation of NETs. To circumvent the limitations of NEs, we developed an NET formation-mediated in situ delivery platform, aLy6G-IFNβ@TLP. Moreover, aLy6G-IFNβ@TLP target NEs in the blood circulation without the need for time-consuming and expensive ex vivo engineering of NEs.

We observed distinct biodistribution patterns in peripheral organs between aLy6G-functionalized and non-functionalized nanoparticles. This difference in biodistribution may be attributed to the NE hitchhiking of aLy6G-IFNβ@TLP. NEs are known to infiltrate various peripheral organs, such as the liver and lungs, under homeostatic conditions[22]. When intravenously injected, aLy6G-IFNβ@TLP traveled through the bloodstream and tissues alongside NEs, resulting in organ distribution profiles resembling those of NEs. Specifically, we observed the distribution of aLy6G-IFNβ@TLP to the liver and lungs, supporting its NE hitchhiking capability. In contrast, the predominant distribution of IFNβ@TLP to the liver is likely due to phagocytosis by liver macrophages of the reticuloendothelial system[23].

For targeted uptake by NEs, the surfaces of TLP were conjugated with aLy6G. Human and murine NEs exhibit difference in surface marker expression. Although we targeted Ly6G, the most well-known surface maker of murine NEs, it is important to note that human NEs do not express Ly6G on their surface[24]. Consequently, before the clinical translation of the aLy6G-IFNβ@TLP system, there is a need to explore which surface receptor should be targeted on human NEs. Furthermore, NEs play a role in MS and constitute a predominant population of CNS-infiltrating cells at specific stages, particularly prior to disease onset and relapse rather than at the established stage. Therefore, customization of aLy6G-IFNβ@TLP treatment is essential, and patients must be carefully monitored for optimal administration periods.

In addition, careful monitoring of kidney and liver functions would be essential in aLy6G-IFNβ@TLP therapy. It has been reported that IFNβ therapy may impact kidney functions and induce hepatic injury[16,25]. IFNβ therapy in clinics settings has shown IFNβ dose-dependent renal failure, such as thrombotic microangiopathy and membranous nephropathy, and liver injury with jaundice[26]. The aLy6G-IFNβ@TLP therapy did not influence kidney and liver function based on blood tests (Supplementary Fig. 15). This may be attributed to the decreased distribution of IFNβ in the kidney and liver in the aLy6G-IFNβ@TLP formulation after intravenous administration.

NET formation in the inflammatory and pathological CNS is a typical and natural feature of the EAE model. In this study, although nanoparticles were delivered to the CNS with the assistance of NET formation, the immune responses triggered by NETs should be carefully evaluated. NETs regulate immunity both directly and indirectly by modulating immune cells. Previous research has shown that NETs upregulate genes encoding IL-6 and pro-IL-1β in macrophages[27]. Additionally, histones, which are major components of NETs, can promote Th17 differentiation and activation[28]. We observed an increased Th17 population in the CNS and spleen of EAE mice

https://doi.org/10.1038/s41467-024-54817-7

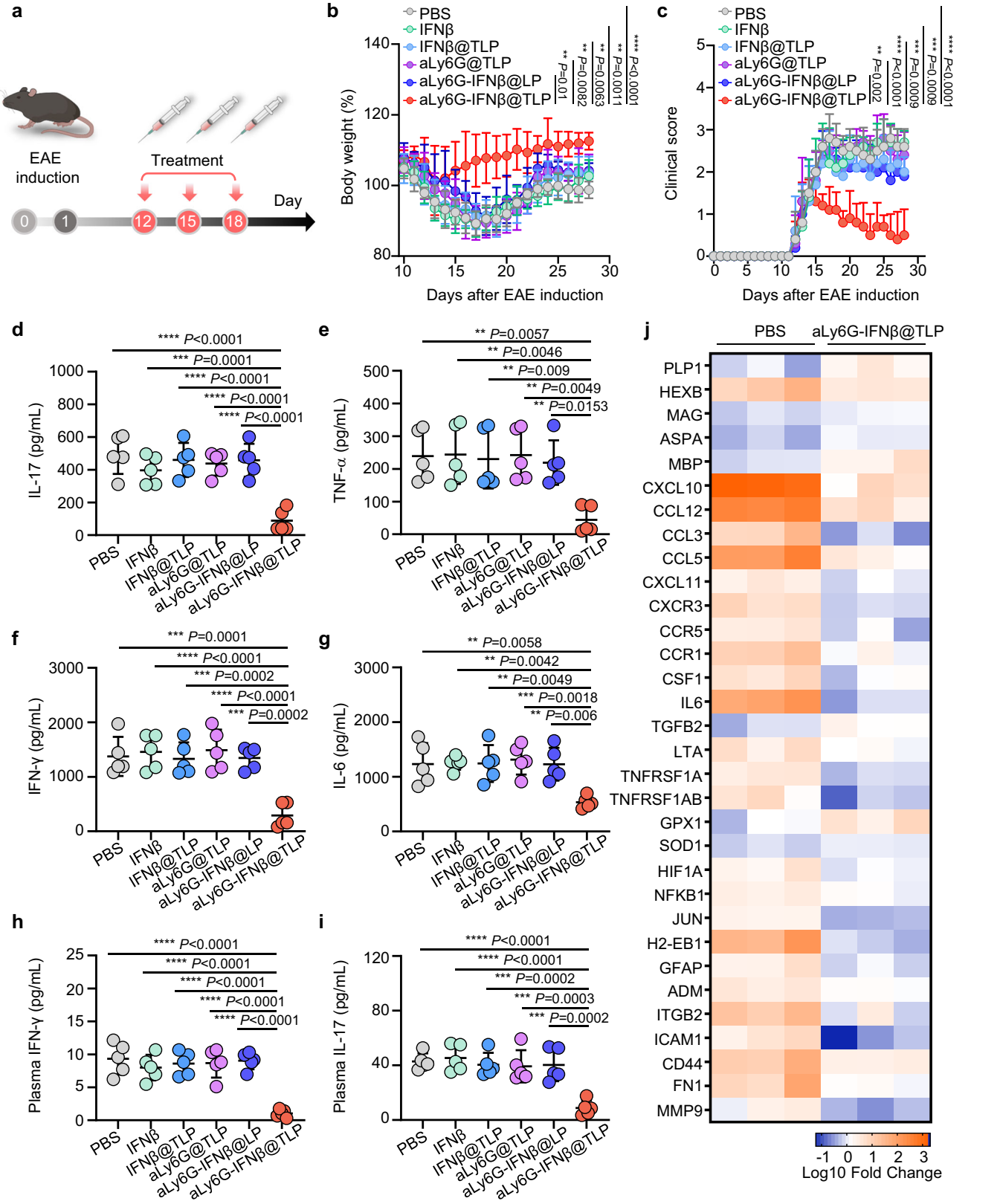

(Supplementary Fig. 16). Pro-inflammatory cytokines such as IL-17, IL-6, and IL-1β were upregulated in the CNS, and some were elevated in peripheral organs, including the spleen, liver, and lungs of EAE mice, which may be mediated by NETs (Supplementary Fig. 17). Furthermore, levels of autoantibodies against NETs in the blood were elevated following EAE immunization (Supplementary Fig. 18), suggesting the induction of NET-mediated autoimmunity. We found that aLy6G-IFNβ@TLP therapy downregulated the levels of IL-17, IL-6, and IL-1β in both the CNS and peripheral organs (Supplementary Fig. 19), as well as autoantibodies against NETs (Supplementary Fig. 20). This effect may be related to the correlation between NE activation and disease progression in EAE.

In conclusion, we designed aLy6G-IFNβ@TLP for in situ NE hitchhiking and delivery of IFNβ to the inflamed CNS. We showed that

Fig. 5 | Therapeutic effect of nanoparticles on EAE. a Schematic illustration of the treatment schedule in the EAE mouse model. Mice were intravenously administered various nanoparticle formulations three times, with three days between each administration, starting from day 12 after EAE immunization. Therapeutic efficacy of various formulations assessed by changes in body weight (**b**) and clinical score (**c**) ($n = 5$ biologically independent samples per group). Statistical significance was analyzed using one-way ANOVA with Tukey's multiple comparisons test. For body weight, $P_{aLy6G\text{-}IFN\beta@TLP\text{-}PBS} < 0.0001$, $P_{aLy6G\text{-}IFN\beta@TLP\text{-}IFN\beta} = 0.0011$, $P_{aLy6G\text{-}IFN\beta@TLP\text{-}IFN\beta@TLP} = 0.0063$, $P_{aLy6G\text{-}IFN\beta@TLP\text{-}aLy6G@TLP} = 0.0082$, $P_{aLy6G\text{-}IFN\beta@TLP\text{-}aLy6G\text{-}IFN\beta@LP} = 0.01$. For clinical score, $P_{aLy6G\text{-}IFN\beta@TLP\text{-}PBS} < 0.0001$, $P_{aLy6G\text{-}IFN\beta@TLP\text{-}IFN\beta} = 0.0009$, $P_{aLy6G\text{-}IFN\beta@TLP\text{-}IFN\beta@TLP} = 0.0009$, $P_{aLy6G\text{-}IFN\beta@TLP\text{-}aLy6G@TLP} < 0.0001$, $P_{aLy6G\text{-}IFN\beta@TLP\text{-}aLy6G\text{-}IFN\beta@LP} = 0.002$. Analysis of IL-17 (**d**), TNF-α (**e**), IFN-γ (**f**), and IL-6 (**g**) production levels of splenocytes after stimulation with $MOG_{35\text{-}55}$ for 72 h at the end of the in vivo experiments ($n = 5$ biologically independent samples per group). Statistical significance was analyzed using one-way ANOVA with Tukey's multiple comparisons test. For IL-17, $P_{aLy6G\text{-}IFN\beta@TLP\text{-}PBS} < 0.0001$, $P_{aLy6G\text{-}IFN\beta@TLP\text{-}IFN\beta} = 0.0001$, $P_{aLy6G\text{-}IFN\beta@TLP\text{-}IFN\beta@TLP} < 0.0001$, $P_{aLy6G\text{-}IFN\beta@TLP\text{-}aLy6G@TLP} < 0.0001$, $P_{aLy6G\text{-}IFN\beta@TLP\text{-}aLy6G\text{-}IFN\beta@LP} < 0.0001$. For TNF-α, $P_{aLy6G\text{-}IFN\beta@TLP\text{-}PBS} = 0.0057$, $P_{aLy6G\text{-}IFN\beta@TLP\text{-}IFN\beta} = 0.0046$, $P_{aLy6G\text{-}IFN\beta@TLP\text{-}IFN\beta@TLP} = 0.009$, $P_{aLy6G\text{-}IFN\beta@TLP\text{-}aLy6G@TLP} = 0.0049$, $P_{aLy6G\text{-}IFN\beta@TLP\text{-}aLy6G\text{-}IFN\beta@LP} = 0.0153$. For IFN-γ, $P_{aLy6G\text{-}IFN\beta@TLP\text{-}PBS} = 0.0001$, $P_{aLy6G\text{-}IFN\beta@TLP\text{-}IFN\beta} < 0.0001$, $P_{aLy6G\text{-}IFN\beta@TLP\text{-}IFN\beta@TLP} = 0.0002$, $P_{aLy6G\text{-}IFN\beta@TLP\text{-}aLy6G@TLP} < 0.0001$, $P_{aLy6G\text{-}IFN\beta@TLP\text{-}aLy6G\text{-}IFN\beta@LP} = 0.0002$. For IL-6, $P_{aLy6G\text{-}IFN\beta@TLP\text{-}PBS} = 0.0058$, $P_{aLy6G\text{-}IFN\beta@TLP\text{-}IFN\beta} = 0.0042$, $P_{aLy6G\text{-}IFN\beta@TLP\text{-}IFN\beta@TLP} = 0.0049$, $P_{aLy6G\text{-}IFN\beta@TLP\text{-}aLy6G@TLP} = 0.0018$, $P_{aLy6G\text{-}IFN\beta@TLP\text{-}aLy6G\text{-}IFN\beta@LP} = 0.006$. Determination of IFN-γ (**h**) and IL-17 (**i**) levels in the plasma at the end of the in vivo experiments ($n = 5$ biologically independent samples per group). Statistical significance was analyzed using one-way ANOVA with Tukey's multiple comparisons test. For plasma IFN-γ, $P_{aLy6G\text{-}IFN\beta@TLP\text{-}PBS} < 0.0001$, $P_{aLy6G\text{-}IFN\beta@TLP\text{-}IFN\beta} < 0.0001$, $P_{aLy6G\text{-}IFN\beta@TLP\text{-}IFN\beta@TLP} < 0.0001$, $P_{aLy6G\text{-}IFN\beta@TLP\text{-}aLy6G@TLP} < 0.0001$, $P_{aLy6G\text{-}IFN\beta@TLP\text{-}aLy6G\text{-}IFN\beta@LP} < 0.0001$. For plasma IL-17, $P_{aLy6G\text{-}IFN\beta@TLP\text{-}PBS} < 0.0001$, $P_{aLy6G\text{-}IFN\beta@TLP\text{-}IFN\beta} < 0.0001$, $P_{aLy6G\text{-}IFN\beta@TLP\text{-}IFN\beta@TLP} = 0.0002$, $P_{aLy6G\text{-}IFN\beta@TLP\text{-}aLy6G@TLP} = 0.0003$, $P_{aLy6G\text{-}IFN\beta@TLP\text{-}aLy6G\text{-}IFN\beta@LP} = 0.0002$. **j** Analysis of mRNA expression levels in the spinal cord associated with the progression of EAE ($n = 3$ biologically independent samples per group). Data are presented as mean ± s.d. Source data are provided as a Source Data file.

aLy6G-IFNβ@TLP can be taken up by NEs, but not by other immune cells, and distribute to the CNS. The release of nanoparticles from NEs via NET formation allowed the delivery of IFNβ at the target sites. Although we used IFNβ for delivery to the CNS in this study, the platform can be applied to deliver other protein drugs to the CNS, leveraging the natural properties of endogenous immunocytes. This approach may hold a great opportunity for the safe and efficient protein drug delivery to various inflammatory CNS disorders.

Methods

Preparation of nanoparticles

Tannic acid nanocore (TC) were first prepared, coated with lipid layer, and conjugated with aLy6G and IFNβ. To prepare TC, the solution of polyvinyl alcohol (m.w. 89,000–98,000, 1 mg/mL, Sigma-Aldrich, St. Louis, MO, USA, cat# 341584) was mixed with an equal volume of tannic acid solution (1 mg/mL, Sigma-Aldrich, cat# 403040). The mixture was then added to a solution of polyethylene glycol (m.w. 8000, Sigma-Aldrich, cat# 1546605) at a weight ratio of 1:24, and incubated for 10 min. The resulting nanoparticles were washed thrice by centrifugation with triple-distilled water (TDW) at 1100 × *g* for 15 min.

In some experiments, Fe^{3+} were incorporated into TC. In brief, $FeCl_3$ solution (10 mg/mL, Sigma-Aldrich, cat# 157740) was added to the polyvinyl alcohol solution at a ratio of 1:5 (w/w), and the mixture was added to the tannic acid solution under stirring. The lipid layer was prepared by mixing 1,2-dipalmitoyl-sn-glycero-3-phospho-(1'-rac-glycerol) (sodium salt) (16:0 PG, Avanti Polar Lipids, Alabaster, AL, USA, cat# 840455), 1,2-dipalmitoyl-sn-glycero-3-phosphocholine (16:0 PC, Avanti Polar Lipids, cat# 850355), and 1,2-distearoyl-sn-glycero-3-phosphoethanolamine-N-[maleimide (polyethylene glycol)−2000] (ammonium salt) (Avanti Polar Lipids, cat# 880126) in chloroform at a molar ratio of 2.8:7:0.2. After removing chloroform by evaporation, the lipid film was hydrated with TC at a weight ratio of 1:7 to form TLP.

For certain experiments, Cy5-conjugated 1,2-dioleoyl-sn-glycero-3-phosphoethanolamine (18:1 Cy5 PE, Avanti Polar Lipids, cat# 810335) was added to the lipid mixture at a molar ratio of 1:1000 and 1:100, respectively. For intravital microscopy imaging, nitrobenzoxadiazole-conjugated 1,2-dioleoyl-sn-glycero-3-phosphoethanolamine (ammonium salt) (18:1 NBD PE, Avanti Polar Lipids, cat# 810145) was added to the lipid mixture at a molar ratio of 1:100.

To prepare aLy6G-IFNβ@TLP, TLP were conjugated with aLy6G and IFNβ via thiol-maleimide chemistry. Briefly, aLy6G (cat# BE0075-1, lot# 854523S1, 807722M1, clone 1A8, Bioxcell, Lebanon, NH, USA) and IFNβ (PBL Assay science, Piscataway, NJ, USA, cat# 12410-1) were functionalized with Traut's reagent (Thermo Fisher Scientific, Waltham, MA, USA, cat# 26101) to incorporate sulfhydryl groups, enabling subsequent conjugation to maleimide moieties. After removing unreacted Traut's reagent from thiolated aLy6G (aLy6G-SH) and thiolated IFNβ (IFNβ-SH) using a 50 kDa and 3 kDa Amicon Ultra filter (Merck Millipore, Burlington, MA, USA, cat# UFC505096, cat# UFC500396), respectively, aLy6G-SH were conjugated to TLP at a ratio of 0.05:1 (w/w), along with 6250 U IFNβ-SH per mg TLP. The resulting product was purified by centrifugation at 27,000 × *g* for 30 min, followed by reconstitution in a 5% glucose solution.

Characterization of nanoparticles

Nanoparticles were characterized by morphology, elemental analysis, size, and surface charge. The morphology and elemental composition of nanoparticles were observed using field emission scanning electron microscope (FE-SEM) (AURIGA; Carl Zeiss, Oberkochen, Germany). The size and surface charge of nanoparticles were measured by dynamic light scattering using an ELSZ-1000 instrument (Otsuka Electronics Co., Osaka, Japan).

Quantification of tannic acid and IFNβ

The tannic acid content in nanoparticles was quantified using the 2,2-diphenyl-1-picrylhydrazyl (DPPH) assay. Nanoparticles (1 mg/mL) were mixed with DPPH (0.2 mM, Sigma-Aldrich, cat# D9132) at a ratio of 1:5 (v/v) and incubated in the dark for 1 h. The absorbance at 517 nm was measured using a UV–vis spectrophotometer (Molecular Devices, San Jose, CA, USA). The amounts of IFNβ were quantified by ELISA. Nanoparticles were centrifuged at 27,000 × *g* for 30 min. Free IFNβ in the supernatant were quantified using a mouse IFNβ ELISA kit (R&D Systems, Minneapolis, MN, USA, cat# DY8234-05), following the manufacturer's instructions. The amounts of IFNβ bound to nanoparticles were calculated by subtraction of free IFNβ from total amounts.

Determination and quantification of aLy6G

The presence of aLy6G conjugated to the surface of nanoparticles was determined by SDS-PAGE and flow cytometry. For SDS-PAGE analysis, free aLy6G and various nanoparticles were mixed with SDS buffer containing 2-mercaptoethanol (GenDEPOT, Katy, TX, USA, cat# L1100-001) for 10 min at 100 °C. Subsequently, samples were loaded onto an SDS-PAGE (10%) gel, followed by staining with Coomassie Brilliant Blue (Bio-Rad, Hercules, CA, USA, cat# 1610436). For flow cytometry, Cy5-labeled nanoparticles were stained with phycoerythrin (PE)-conjugated anti-rat IgG antibody (1:10, cat# 405406, lot# B338568, clone Poly4054, BioLegend, San Diego, CA, USA) for 1 h. The fluorescence signals of nanoparticles and aLy6G were observed using a CytoFLEX LX Flow Cytometer (Beckman Coulter, Brea, CA, USA). For aLy6G quantification, nanoparticles were centrifuged at 27,000 × *g* for 30 min, the supernatant was collected, and free aLy6G were quantified using a rat

https://doi.org/10.1038/s41467-024-54817-7

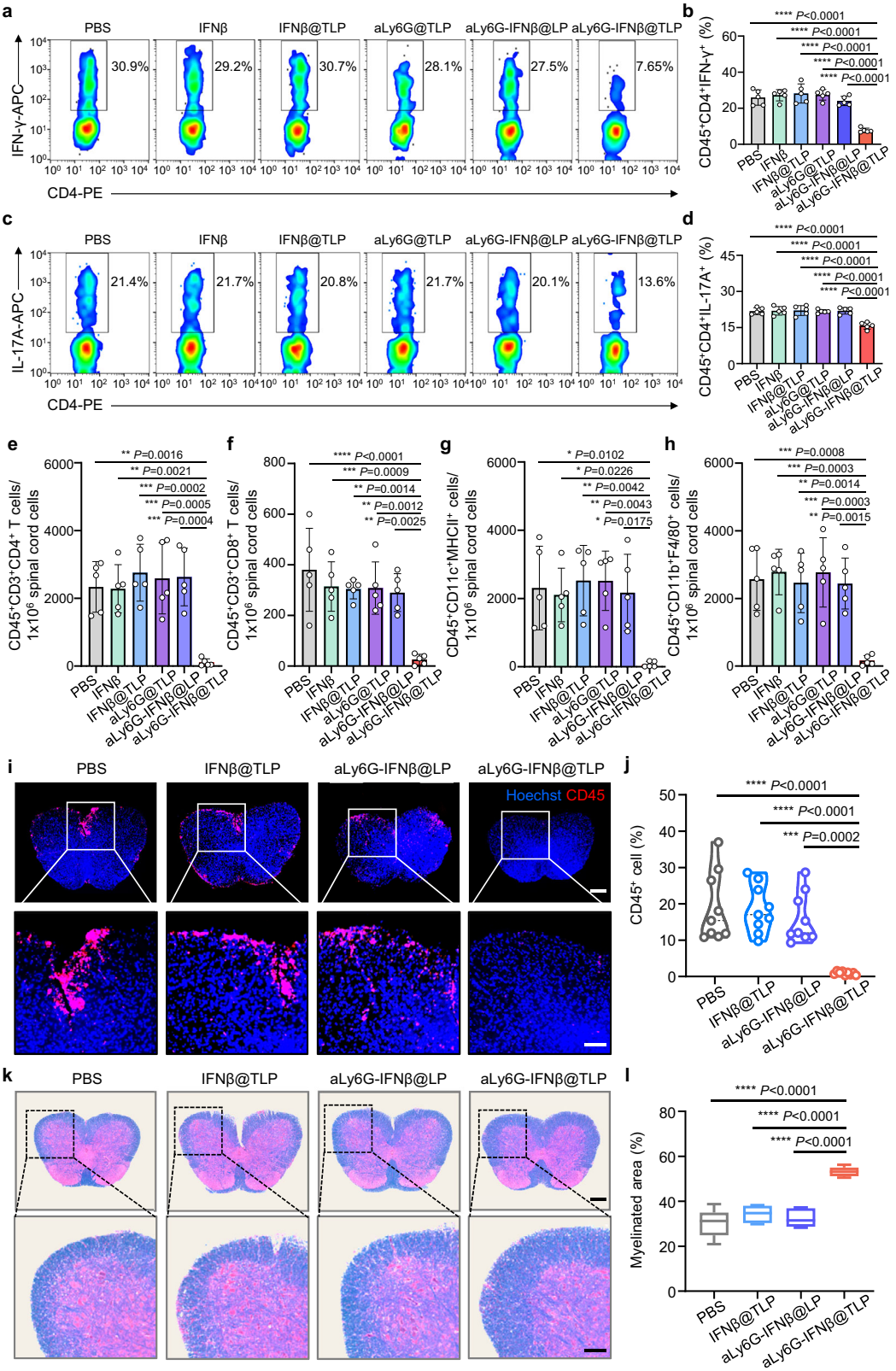

IgG ELISA kit (Abcam, Cambridge, UK, cat# ab157737), following the manufacturer's instructions.

Analysis of radical scavenging activity

The radical scavenging activity of nanoparticles was analyzed using fluorimetric and colorimetric assays. The scavenging of superoxide anion was evaluated using the nitro blue tetrazolium test. In brief, a solution containing nitro blue tetrazolium (75 μM, Cayman chemical, Ann Arbor, MI, USA, cat# 17341), riboflavin (20 μM, Sigma-Aldrich, cat# 1603006), and l-methionine (12.5 mM, Sigma-Aldrich, cat# M5308) in PBS (pH 7.4) was mixed with various concentrations of nanoparticles, followed by incubation under ultraviolet irradiation for 15 min. The absorbance was analyzed using a Microplate Reader (Molecular Devices). The scavenging of hydroxyl radical was assessed using

Fig. 6 | Recovery of the CNS inflammation by nanoparticles. Various nanoparticle formulations were intravenously administered 12 days after EAE immunization, repeating every three days for a total of three administrations. Spinal cord was collected and analyzed at 28 days post-immunization. **a** Representative flow cytometry data of Th1 in the spinal cord. **b** Relative quantification of Th1 in the spinal cord ($n = 5$ biologically independent samples per group). Statistical significance was analyzed using one-way ANOVA with Tukey's multiple comparisons test. $P_{aLy6G\text{-}IFN\beta@TLP\text{-}PBS} < 0.0001$, $P_{aLy6G\text{-}IFN\beta@TLP\text{-}IFN\beta} < 0.0001$, $P_{aLy6G\text{-}IFN\beta@TLP\text{-}IFN\beta@TLP} < 0.0001$, $P_{aLy6G\text{-}IFN\beta@TLP\text{-}aLy6G@TLP} < 0.0001$, $P_{aLy6G\text{-}IFN\beta@TLP\text{-}aLy6G\text{-}IFN\beta@LP} < 0.0001$. **c** Representative flow cytometry data of Th17 in the spinal cord. **d** Relative quantification of Th17 in the spinal cord ($n = 5$ biologically independent samples per group). Statistical significance was analyzed using one-way ANOVA with Tukey's multiple comparisons test. $P_{aLy6G\text{-}IFN\beta@TLP\text{-}PBS} < 0.0001$, $P_{aLy6G\text{-}IFN\beta@TLP\text{-}IFN\beta} < 0.0001$, $P_{aLy6G\text{-}IFN\beta@TLP\text{-}IFN\beta@TLP} < 0.0001$, $P_{aLy6G\text{-}IFN\beta@TLP\text{-}aLy6G@TLP} < 0.0001$, $P_{aLy6G\text{-}IFN\beta@TLP\text{-}aLy6G\text{-}IFN\beta@LP} < 0.0001$. Quantification of infiltrated helper T cells ($CD45^+CD3^+CD4^+$) (**e**), cytotoxic T cells ($CD45^+CD3^+CD8^+$) (**f**), DCs ($CD45^+CD11c^+MHCII^+$) (**g**), and macrophages ($CD45^+CD11b^+F4/80^+$) (**h**) in the spinal cord ($n = 5$ biologically independent samples per group). Statistical significance was analyzed using one-way ANOVA with Tukey's multiple comparisons test. For helper T cells, $P_{aLy6G\text{-}IFN\beta@TLP\text{-}PBS} = 0.0016$, $P_{aLy6G\text{-}IFN\beta@TLP\text{-}IFN\beta} = 0.0021$, $P_{aLy6G\text{-}IFN\beta@TLP\text{-}IFN\beta@TLP} = 0.0002$, $P_{aLy6G\text{-}IFN\beta@TLP\text{-}aLy6G@TLP} = 0.0005$, $P_{aLy6G\text{-}IFN\beta@TLP\text{-}aLy6G\text{-}IFN\beta@LP} = 0.0004$. For cytotoxic T cells, $P_{aLy6G\text{-}IFN\beta@TLP\text{-}PBS} < 0.0001$, $P_{aLy6G\text{-}IFN\beta@TLP\text{-}IFN\beta} = 0.0009$, $P_{aLy6G\text{-}IFN\beta@TLP\text{-}IFN\beta@TLP} = 0.0014$, $P_{aLy6G\text{-}IFN\beta@TLP\text{-}aLy6G@TLP} = 0.0012$, $P_{aLy6G\text{-}IFN\beta@TLP\text{-}aLy6G\text{-}IFN\beta@LP} = 0.0025$. For DCs, $P_{aLy6G\text{-}IFN\beta@TLP\text{-}PBS} = 0.0102$, $P_{aLy6G\text{-}IFN\beta@TLP\text{-}IFN\beta} = 0.0226$, $P_{aLy6G\text{-}IFN\beta@TLP\text{-}IFN\beta@TLP} = 0.0042$, $P_{aLy6G\text{-}IFN\beta@TLP\text{-}aLy6G@TLP} = 0.0043$, $P_{aLy6G\text{-}IFN\beta@TLP\text{-}aLy6G\text{-}IFN\beta@LP} = 0.0175$. For macrophages, $P_{aLy6G\text{-}IFN\beta@TLP\text{-}PBS} = 0.0008$, $P_{aLy6G\text{-}IFN\beta@TLP\text{-}IFN\beta} = 0.0003$, $P_{aLy6G\text{-}IFN\beta@TLP\text{-}IFN\beta@TLP} = 0.0014$, $P_{aLy6G\text{-}IFN\beta@TLP\text{-}aLy6G@TLP} = 0.0003$, $P_{aLy6G\text{-}IFN\beta@TLP\text{-}aLy6G\text{-}IFN\beta@LP} = 0.0015$. **i** Representative CD45 staining in the spinal cord of EAE mice. Scale bar: 250 μm. Scale bar of expanded microscopic image: 125 μm. **j** Quantification of CD45-positive cells in three selected fields per sample from immunofluorescence images ($n = 3$ biologically independent samples per group). Statistical significance was analyzed using one-way ANOVA with Tukey's multiple comparisons test. $P_{aLy6G\text{-}IFN\beta@TLP\text{-}PBS} < 0.0001$, $P_{aLy6G\text{-}IFN\beta@TLP\text{-}IFN\beta@TLP} < 0.0001$, $P_{aLy6G\text{-}IFN\beta@TLP\text{-}aLy6G\text{-}IFN\beta@LP} = 0.0002$. **k** Representative LFB staining of spinal cord revealing areas of myelination. Scale bar: 250 μm. Scale bar of expanded microscopic image: 125 μm. **l** Quantification of myelinated area from LFB staining images ($n = 5$ biologically independent samples per group). Statistical significance was analyzed using one-way ANOVA with Tukey's multiple comparisons test. $P_{aLy6G\text{-}IFN\beta@TLP\text{-}PBS} < 0.0001$, $P_{aLy6G\text{-}IFN\beta@TLP\text{-}IFN\beta@TLP} < 0.0001$, $P_{aLy6G\text{-}IFN\beta@TLP\text{-}aLy6G\text{-}IFN\beta@LP} < 0.0001$. Data are presented as mean ± s.d. Source data are provided as a Source Data file.

terephthalic acid. A solution containing terephthalic acid (0.5 mM, Sigma-Aldrich, cat# 40818) and H_2O_2 (2 mM, Sigma-Aldrich, cat# 216763) in PBS (pH 7.4) was mixed with various concentrations of nanoparticles in the dark for 12 h. The fluorescence spectrum was analyzed using a Microplate Reader with a 315 nm excitation.

In vitro IFNβ release test

The IFNβ release profile was assessed in FBS (GenDEPOT, cat# F50900-050) and PBS. Aliquots (0.1 mL) were collected at various time points, with the same volume of FBS or PBS replenished after each collection. The aliquots were centrifuged at 27,000 × *g* for 30 min, and the supernatant was collected. The amount of released IFNβ was quantified using a mouse IFNβ ELISA kit (R&D Systems), following the manufacturer's instructions.

Stability test of IFNβ on nanoparticles

The stability of IFNβ on nanoparticles was evaluated by incubating nanoparticles in H_2O_2 solution. The samples were incubated in 10 μM H_2O_2 solution at 4 °C for 3 h, followed by centrifugation at 27,000 × *g* for 30 min. Nanoparticles were then resuspended in FBS and incubated at 4 °C for 72 h. Samples were centrifuged at 27,000 × *g* for 30 min, and the concentration of IFNβ was measured using a mouse IFNβ ELISA kit.

Animals

Female C57BL/6 mice (Raon Bio Co., Gyeonggido, Republic of Korea) were kept in a specific-pathogen-free room with a temperature maintained at 22 ± 2 °C and humidity at 55 ± 5% (Animal Center for Pharmaceutical Research, College of Pharmacy, Seoul National University, Seoul, Republic of Korea). Mice were housed in groups of up to five per cage, maintained on a 12 h light/dark cycle, with ad libitum access to food (Rodent Chow; Cat# 38057, Purina Lab, Missouri, USA) and water. Daily monitoring was conducted to evaluate general health, behavior, and any signs of distress in the mice. At the predetermined endpoints of the experiments, mice were humanely euthanized by CO_2 inhalation. The animal study protocol (SNU-230226-1-1) was approved by the Animal Care and Use Committee of Seoul National University. All animal experiments were conducted in accordance with relevant ethical regulations.

Isolation of mouse NEs

Mouse NEs were isolated from mouse bone marrow using a density gradient centrifugation method[29]. After removing the skin and muscles from the femur and tibia, the bones were immersed in 70% ethanol, followed by washing. The bone marrow cells were flushed with complete Roswell Park Memorial Institute (RPMI) medium (Welgene, Gyeongsan-si, Republic of Korea, cat# LM 001-05) supplemented with 10% FBS (v/v), 100 U/mL of penicillin, and 100 μg/mL of streptomycin (Capricorn Scientific, cat# PS-B), and then centrifuged at 410 × *g* for 7 min. Red blood cells were removed using ACK lysing buffer (Thermo Fisher Scientific, cat# A1049201), followed by the addition of PBS and centrifugation. The cell pellets were resuspended and overlaid on top of the Histopaque solution, consisting of 3 mL of Histopaque 1077 (Sigma-Aldrich, cat# 10771) and 3 mL of Histopaque 1119 (Sigma-Aldrich, cat# 11191). After centrifugation at 840 × *g* for 30 min, NEs were collected at the interface of the Histopaque 1077 and Histopaque 1119 layers and washed with complete RPMI. The purity and yield were analyzed using a BD FACSLyric Flow Cytometer (BD Biosciences). As antibodies, Ly6G FITC (1:100, cat# 127606, lot# B277117, clone 1A8, BioLegend) and CD11b PE (1:100, cat# 101208, lot# B313035, clone M1/70, BioLegend) were used.

Assessment of intracellular ROS scavenging

Intracellular ROS scavenging activity was assessed using chemiluminescence and fluorescence method. NEs were seeded at a density of 1×10^5 cells per well in 24-well plates and incubated with aLy6G-IFNβ@LP (0.14 mg/mL) and aLy6G-IFNβ@TLP (0.32 mg/mL) for 1 h. For the chemiluminescence assay, the cells were mixed with a solution containing luminol (10 μg/mL, Sigma-Aldrich, cat# 123072) and horseradish peroxidase (6 U/mL, Sigma-Aldrich, cat# P8375). Luminescence was detected in the absence or presence of PMA (100 nM, Sigma-Aldrich, cat# 79346) using a Microplate Reader (Molecular Devices). In the fluorescent method, NEs were treated with aLy6G-IFNβ@LP (0.14 mg/mL) and aLy6G-IFNβ@TLP (0.32 mg/mL) for 1 h, followed by incubation with CM-H2DCFDA (Invitrogen, Carlsbad, CA, USA, cat# C6827) and PMA for 5 min. The cells were washed, and the fluorescence was analyzed using flow cytometry.

In vitro study of NE viability

The viability of NEs incubated with nanoparticles was assessed using a luminescent cell viability assay. NEs were seeded at a density of 1×10^5 cells per well in 24-well plates and treated with diluted nanoparticles at 37 °C. Cell viability was measured using the CellTiter-Glo Luminescent Cell Viability Assay (Promega, Madison, WI, USA, cat# G7570) following the manufacturer's instructions.

Evaluation of binding of nanoparticles on NEs

The binding capacity of nanoparticles on NEs and other immune cells was assessed using flow cytometry. NEs were seeded onto a 24-well plate at a density of 1×10^5 cells per well, treated with 0.32 mg/mL of Cy5-labeled nanoparticles, and incubated for 1 h. Cells were stained with the following antibodies: Gr-1 FITC (1:100, cat# 108405, lot# B353671, clone RB6-8C5, BioLegend) and CD11b PE (1:100, cat# 101208, lot# B313035, clone M1/70, BioLegend). For the analysis of nanoparticle binding to other immune cells, splenocytes were utilized. Red blood cells were removed using an ACK lysis buffer. The resulting single-cell suspension was treated with Cy5-labeled nanoparticles for 1 h and stained with the following antibodies: MHCII PerCP/Cy5.5 (1:100, cat# 107626, lot# B353671, clone M5/114.15.2, BioLegend), CD3 FITC (1:100, cat# 100204, lot# B351638, clone 17A2, BioLegend), CD11c FITC (1:100, cat# 117306, lot# B353146, clone N418, BioLegend), F4/80 FITC (1:100, cat# 123108, lot# B407719, clone BM8, BioLegend), and CD19 PE (1:100, cat# 115507, lot# B363910, clone 6D5, BioLegend). The binding of nanoparticles to NEs, and immune cells was analyzed using a BD FACSLyric Flow Cytometer.

Endocytosis mechanism study

To investigate the endocytosis mechanism of nanoparticles, NEs were seeded onto a 24-well plate at a density of 1×10^5 cells per well and treated with various internalization inhibitors. NEs were incubated with chlorpromazine (28 mM, Sigma-Aldrich, cat# C8138), chloroquine (10 μM, Sigma-Aldrich, cat# C-6628), methyl-β-cyclodextrin (5 mM, Sigma-Aldrich, ca# C4555), amiloride (50 μM, Sigma-Aldrich, cat# A7410), and cytochalasin D (5 μM, Sigma-Aldrich, cat# C8273) for 1 h at 37 °C. Cy5-labeled aLy6G-IFNβ@TLP (0.32 mg/mL) were then added and incubated for 3 h. The internalization of nanoparticles was analyzed by flow cytometry.

Chemotactic migration study

To evaluate the chemotaxis of aLy6G-IFNβ@TLP-bound NEs, an in vitro BBB model was employed. bEnd.3 cells (ATCC, cat# CRL-2299) were seeded at a density of 1×10^5 cells onto the upper chamber of a transwell insert (polycarbonate membrane, 3 μm pore size, 0.33 cm^2 surface area, SPL Life Sciences, Pocheon-si, Republic of Korea, cat# 37124), pre-coated with collagen I (10 μg/cm^2, CORNING, Corning, NY, USA cat# 354236), and cultured for 7 days in complete Dulbecco's Modified Eagle Medium (DMEM) medium (Welgene, cat# LM 001-05) supplemented with 10% FBS (v/v), 100 U/mL of penicillin, and 100 μg/mL of streptomycin. NEs (2×10^5 cells) and Cy5-labelld nanoparticles were added to the upper chamber, while FBS-free RPMI medium with fMLP (10 nM, Sigma-Aldrich, cat# F3506) was added to the lower chamber, and incubated for 3 h. NE migration (%) represented the proportion of NEs in the lower chamber relative to the total number of NEs initially introduced into the upper chamber. For confocal microscopy analysis, cells in the lower chamber were harvested, seeded on the poly-l-lysine-coated coverslips (CORNING), and stained with Hoechst 33342 (Sigma-Aldrich, cat# B2261) at room temperature for 10 min. Fluorescence images were acquired using a Leica TCS8 confocal microscope (Leica Microsystems).

In vitro study of NET formation-mediated nanoparticle release

To test NET formation-mediated release of nanoparticles, NEs were seeded onto a 24-well plate at a density of 1×10^5 cells and treated with Cy5-labeled nanoparticles (0.32 mg/mL) for 1 h. For confocal microscopy, cells were seeded onto poly-l-lysine-coated coverslips and treated with PMA (500 nM). Extracellular MPO and nucleic acid were stained with rabbit anti-MPO antibody (1:500, cat# ab208670, lot# GR3390666-4, Abcam) and Sytox Green (Thermo Fisher Scientific), followed by staining with Cy3-anti-rabbit IgG antibody (1:100, cat# ab97075, lot# GR3385714-2, Abcam). Fluorescence images were captured with a Leica TCS8 confocal microscope.

NET formation-mediated nanoparticle release was also visualized using SEM and transmission electron microscopy (TEM). For SEM imaging, NEs were treated with Fe-labeled nanoparticles (0.32 mg/mL) for 1 h, seeded on poly-l-lysine-coated coverslips, and treated with PMA (500 nM) for 4 h, followed by fixing with Karnovsky's fixative solution. Cells were washed with sodium cacodylate buffer (0.05 M) and incubated with 1% osmium tetroxide solution at 4 °C for 1 h. Cells were washed and dehydrated with a series of ethanol solutions, followed by drying with hexamethyldisilazane. Coverslips were sputter-coated with 1.5 nm platinum and imaged using a field-emission SEM (AURIGA; Carl Zeiss, Oberkochen, Germany). Elemental mapping was performed using SEM with energy-dispersive X-ray spectroscopy (EDS).

For TEM imaging, NEs were treated with Fe-labeled nanoparticles for 1 h, followed by incubation with PMA (500 nM). Cells were fixed with Karnovsky's fixative solution. After washing with sodium cacodylate buffer (0.05 M), cell pellets were fixed with 1% osmium tetroxide solution, and stained with 0.5% uranyl acetate overnight. Cell pellets were embedded in Spurr's resin, sectioned at 60 nm thickness, and observed under a JEM1010 TEM.

Biodistribution study of nanoparticles in EAE mouse model

The biodistribution of nanoparticles was assessed in the EAE mouse model. Female C57BL/6 mice (11 weeks old) were subcutaneously injected with 200 μg of MOG_{35-55} peptide (2 mg/mL, Prospec, Rehovot, Israel, cat# PRO-371), emulsified with an equal volume of Complete-Freund's adjuvant (CFA) (Chondrex, Woodinville, WA, USA, cat# 7001), consisting of 4 mg/mL of heat-killed *M. Tuberculosis* H37 RA. Subsequently, the mice received 400 ng of Pertussis toxin (PTX) (List Biological Labs, Campbell, CA, USA, cat# 180) intraperitoneally at 2 and 24 h post-injection of the emulsion. Intravenous injection of Cy5-labeled nanoparticles at a dose of 40 mg per kg was performed on day 12 post-immunization. The fluorescence of nanoparticles in the brain, spinal cord, and major organs was assessed using an IVIS spectrum In Vivo Imaging System (PerkinElmer) at various time points post-injection.

For the analysis of the internalization of nanoparticles in NEs, spinal cords were digested using collagenase I (Sigma-Aldrich, cat# C0130). The resulting single-cell suspension was stained with the following antibodies: CD45 PerCP/Cy5.5 (1:100, cat# 103132, lot# B426652, clone 30-F11, BioLegend), Ly6G FITC (1:100, cat# 127606, lot# B277117, clone 1A8, BioLegend), and CD11b PE (1:100, cat# 101208, lot# B313035, clone M1/70, BioLegend). To assess the internalization of nanoparticles in other immune cells, high-dimensional flow cytometry analysis was conducted. Single-cell suspensions of spinal cord were stained with the following antibodies: CD45 BV421 (1:100, cat# 103133, clone 30-F11, BioLegend), CD3 PE (1:100, cat# 100205, lot# B375691, clone 17A2, BioLegend), CD11b BV605 (1:100, cat# 101257, lot# B363316, clone M1/70, BioLegend), Ly6G PE/Cy7 (1:100, cat# 127617, lot# B371539, clone 1A8, BioLegend), and MHCII Alexa Fluor 488 (1:100, cat# 107615, clone M5/114.15.2, BioLegend). Flow cytometry data were obtained with a BD FACSLyric Flow Cytometer and processed using FlowJo software (FlowJo, Ashland, OR, USA). CD45-positive immune cell numbers were standardized to 10,000, and dimensionality reduction was employed using the t-distributed stochastic neighbor embedding (t-SNE) method.

For confocal microscopy, spinal cord was embedded in Tissue-Tek O.C.T. medium (Sakura Finetek, Torrance, CA, USA, cat# 4583), and sectioned at 10 μm thickness (CM3050S; Leica Biosystems). Tissue sections were stained with FITC-conjugated anti-mouse Ly6G antibody (1:100, cat# 127606, lot# B277117, clone 1A8, BioLegend) and Hoechst 33342. Fluorescence images were acquired using a Leica TCS8 confocal microscope.

Intravital microscopy

To visualize nanoparticle infiltration into spinal cords, in vivo live-imaging of spinal cords was conducted. EAE mice were anaesthetized

by intraperitoneally injecting avertin, followed by exposing the thoracic region of the spinal cord through the careful removal of subcutaneous connective tissues and muscles. Subsequently, the mice were intravenously administered NBD-labeled nanoparticles at a dose of 40 mg per kg and 200 mg per kg of rhodamine B isothiocyanate (RITC)–dextran (70 kDa, Sigma-Aldrich, cat# R9379) for blood vessel labeling. The mice were transferred to a preheated chamber and maintained at 37 °C during the imaging studies. The spinal cord was imaged using an Olympus FVMPE-RS multiphoton laser scanning microscope with a × 25 water-immersion objective lens (Olympus, Tokyo, Japan) at selected time points.

In vivo efficacy test

To evaluate therapeutic efficacy, EAE mice were intravenously administered with various nanoparticles at a dose of 5000 U of IFNβ per mouse, starting on day 12 and repeated every three days for a total of three doses. Symptoms and body weight were monitored daily, starting from day 10 post-immunization. In experiments comparing dose-dependent treatments, EAE mice were treated with nanoparticles loaded with IFNβ at doses of 1000 U, 2500 U, and 5000 U, starting on day 12 and administered at three-day intervals for a total of three doses. In experiments comparing the start date of administration, EAE mice received nanoparticles containing 5000 U of IFNβ, starting on either day 0 or day 12, with treatments at three-day intervals for three doses. In experiments comparing dosage frequency, EAE mice were treated with nanoparticles loaded with 5000 U of IFNβ following different frequency regimens, starting from day 12. EAE scores were assigned on a scale from 0 to 5 using the following criteria: 0, no disease; 0.5, partially limp tail; 1, limp tail; 1.5, limp tail and hind leg impairment; 2, limp tail and weakness of hind legs; 2.5, one hind limb paralyzed; 3, limp tail and complete paralysis of hind limb; 3.5, paralyzed hind limbs, weakness in forelimbs; 4, forelimbs paralyzed; 5, dying or dead[30].

Cytokine analysis

Cytokine levels in blood, splenocytes, and organs were assessed by ELISA. For plasma samples, IFN-γ, IL-17, and IL-6 levels were quantified using ELISA kits according to the manufacturer's instructions (R&D Systems, cat# DY485, cat# DY421, cat# DY406). For restimulated splenocytes, spleens were harvested, meshed, and filtered through a 40 μm cell strainer. Red blood cells were lysed using ACK lysis buffer. Splenocytes were seeded in a 96-well plate at a density of 2×10^6 cells per well and incubated with 10 μg/mL of MOG_{35-55} for 72 h at 37 °C. Levels of IFN-γ, IL-17, IL-6, and TNF-α were measured using ELISA kits. For organ samples, tissues were extracted and homogenized in PBS supplemented with a protease inhibitor, following the manufacturer's instructions (Roche, Basel, Switzerland, cat# 11836170001). The samples were then centrifuged at 13,000 × *g* for 30 min, and levels of IL-17, IL-1β, and IL-6 were quantified using ELISA kits (R&D Systems).

Profiling of gene expression in the spinal cord

Gene expression associated with the development of EAE was evaluated by reverse transcription-polymerase chain reaction (RT-PCR). Mice were euthanized, and the spinal cord was extracted on day 28 after EAE immunization. The spinal cord was homogenized in 1 mL Trizol reagent (Invitrogen, cat# 15596018), and mRNA was extracted following the manufacturer's instructions. cDNA was synthesized using a Maxime™ RT PreMix (iNtRON Biotechnology, Seongnam-si, Republic of Korea, cat# 25081). Quantitative PCR was performed using an Applied Biosystems 7300 Real-Time PCR System. The primers used in the RT-PCR were provided from the AccuTarget™ qPCR Screening Kit (Bioneer, cat# SM-0000-10 0108).

Evaluation of immune cell infiltration in the spinal cord

Immune cell infiltration into the spinal cord was evaluated on day 28 after immunization by flow cytometry. Spinal cords were harvested, digested with collagenase, and filtered through a 40 μm cell strainer. For intracellular IFN-γ and IL-17A analysis, single-cell suspensions were stimulated PMA (50 ng/mL), ionomycin (1 μM, Sigma-Aldrich, cat# I0634), and Brefeldin-A (10 μg/mL, BioLegend, cat# 420601) for 4 h, followed by staining with antibodies and analysis using a BD FACSLyric Flow Cytometer. The following antibodies were used: CD45 PerCP/Cy5.5 (1:100, cat# 103132, lot# B426652, clone 30-F11, BioLegend), CD4 PE (1:100, cat# 116006, lot# B370907, clone RM4-4, BioLegend), IFN-γ APC (1:100, cat# 505810, lot# B290393, clone XMG1.2, BioLegend), IL-17A APC (1:100, cat# 506916, lot# 358441, clone TC11-18H10.1, BioLegend), CD11c PE (1:100, cat# 117307, lot# B374561, clone N418, BioLegend), MHCII APC (1:100, cat# 107614, lot# B312899, clone M5/114.15.2, BioLegend), CD11b PE (1:100, cat# 101208, lot# B313035, clone M1/70, BioLegend), F4/80 APC (1:100, cat# 123116, lot# B336912, clone BM8, BioLegend), and CD8a PerCP/Cy5.5 (1:100, cat# 100734, lot# B292848, clone 53-6.7, BioLegend). The gating strategy is shown in Supplementary Fig. 21.

Study of nanoparticle effect on neuroglia

The effects of nanoparticles on astrocytes and microglia were evaluated using RT-PCR, flow cytometry, and immunofluorescence staining. Astrocytes were isolated following a previously described protocol with slight modifications[31]. For astrocyte isolation, spinal cord single-cell suspensions were stained with the following antibodies for sorting: CD45R/B220 PE (1:200, cat# 103207, lot# B411979, clone RA3-6B2, BioLegend), TER-119 PE (1:200, cat# 116207, lot# B392792, clone TER-119, BioLegend), O4 PE (1:100, cat# 130-117-507, lot# 5240701123, clone O4, Miltenyi Biotec), CD105 PE (1:200, cat# 120407, lot# B364575, clone MJ7/18, BioLegend), CD140a PE (1:200, cat# 135905, lot# B401844, clone APA5, BioLegend), Ly6G PE (1:200, cat# 164503, lot# B417691, clone S19018G, BioLegend), Ly6C APC/Cy7 (1:200, cat# 128025, lot# B417977, clone HK1.4, BioLegend), CD45 Alexa Fluor 647 (1:100, cat# 103124, lot# B364327, clone 30-F11, BioLegend), CD11c FITC (1:100, cat# 117306, lot# B353146, clone N418, BioLegend), and CD11b BV605 (1:100, cat# 101257, lot# B363316, clone M1/70, BioLegend). Astrocytes were gated as $Ter119^-O4^-CD45R^-CD140a^-CD105^-Ly6G^-CD45^-CD11b^-CD11c^-Ly6C^-$ and sorted using a FACSAria III (BD Biosciences). The gating strategy is shown in Supplementary Fig. 13a.

For RT-PCR, total RNA from astrocytes was isolated using Trizol reagent, followed by cDNA synthesis with Maxime™ RT PreMix. Gene expression was quantified using TOPreal SYBR Green qPCR High-ROX PreMIX (Enzynomics, Daejeon, Republic of Korea, cat# RT501M). The primer sequences used are listed in Supplementary Table 1.

For flow cytometric analysis of microglia, spinal cord single-cell suspensions were stained with the following antibodies: CD11b PE (1:100, cat# 101208, lot# B313035, clone M1/70, BioLegend), CD45 PerCP/Cy5.5 (1:100, cat# 103132, lot# B426652, clone 30-F11, BioLegend), CD40 APC (1:100, cat# 124612, lot# B351628, clone 3/23, BioLegend), CD86 APC (1:100, cat# 105011, lot# B268255, clone GL-1, BioLegend), and CD68 APC (1:100, cat# 137003, lot# B352984, clone AF-11, BioLegend). Cells were analyzed using a BD FACSLyric flow cytometer. The gating strategy is shown in Supplementary Fig. 14a.

For immunofluorescence staining, spinal cords were embedded in O.C.T. compound, and 10 μm sections were prepared. Sections were permeabilized and blocked with 3% BSA and 0.3% Triton X-100 for 1 h. The sections were then incubated overnight at 4 °C with rabbit anti-GFAP antibody (1:200, cat# 80788S, lot# 2, Cell Signaling Technology, Denver, MA, USA) or rabbit anti-Iba1 antibody (1:50, cat# 17198S, lot# 6, Cell Signaling Technology), followed by incubation with Alexa Fluor 488-conjugated anti-rabbit IgG (1:200, cat# ab150077, lot# 1052444-22, Abcam) for 1 h. Images were obtained using a Leica TCS8 confocal microscope.

Evaluation of NET formation in the peripheral organs and CNS

Organs were fixed in 10% (v/v) formalin for 24 h at 4 °C, embedded in Tissue-Tek O.C.T. medium, frozen, and sectioned at a thickness of

10 µm. Tissue sections were blocked with 1% BSA in 0.1% Tween 20 in PBS at room temperature for 30 min. The sections were then stained overnight at 4 °C with a rabbit anti-citrullinated histone H3 antibody (1:200, cat# NB100-57135, lot# 24E23, Novus Biologicals, Minneapolis, MN, USA). After staining, sections were washed and then stained with Cy3-conjugated anti-rabbit IgG (1:100, cat# ab97075, lot# GR3385714-2, Abcam) for 1 h. After washing, the sections were incubated with Hoechst 33342 to counterstain the nuclei. Images were acquired using a Leica TCS8 confocal microscope. For NET quantification, NETs were counted in three sections per sample, with five mice per group evaluated. The NET area was analyzed using ImageJ software (National Institutes of Health).

Analysis of anti-NET IgG and IgM

Anti-NET IgG and IgM levels in plasma were quantified using a NET ELISA assay, as previously described[32]. For NET-coated immunoplate preparation, NEs were isolated from mouse bone marrow, resuspended in RPMI medium supplemented with 3% FBS (v/v), 100 U/mL penicillin, and 100 µg/mL streptomycin, and seeded in a 6-well plate at a density of 3×10^6 NEs per well. To generate NETs, NEs were treated with PMA (500 nM) for 4 h at 37 °C. After treatment, NETs adhered to the well plate were washed with cold PBS. The solution was then centrifuged at $450 \times g$ for 10 min. The cell-free supernatant was then centrifuged at $16{,}000 \times g$ for 10 min to pellet the NETs. The NET pellet was washed with cold PBS, centrifuged again, and resuspended in cold PBS at a concentration corresponding to 2×10^8 NEs/mL. NETs were partially digested with micrococcal nuclease (10 U/mL, New England Biolabs, Ipswich, MA, USA) for 20 min at 37 °C. The reaction was stopped by adding EDTA (15 mM). The protein concentration of NETs was measured using a Bicinchoninic Acid Protein Assay Kit (ThermoFisher Scientific, cat# 23225).

A 96-well immunoplate was coated with 5 µg/mL of digested NETs diluted in bicarbonate buffer (0.05 M) and incubated overnight at 4 °C. The plate was then blocked with 1% bovine serum albumin (BSA) (GenDEPOT, cat# A0100-010) in PBS for 1 h. Plasma samples, diluted 1:10 in blocking buffer, were added to individual wells and incubated for 2 h. After washing, the plate was incubated with horseradish peroxidase-conjugated anti-mouse IgG (1:400, cat# sc-516102, lot# K2019, Santa Cruz Biotechnology, Dallas, TX, USA) or horseradish peroxidase-conjugated anti-mouse IgM (1:10,000, cat# ab97230, lot# 1028601-9, Abcam) for 2 h. The plate was reacted with a 1:1 (v/v) mixture of H_2O_2 and tetramethylbenzidine (R&D system, cat# DY999B). Absorbance was measured at a wavelength of 450 nm using a Microplate Reader (Molecular Devices).

Flow cytometric analysis of Th17

The spinal cord and brain were digested with collagenase, and filtered through a 40 µm cell strainer to obtain single-cell suspensions. The spleen was meshed, and red blood cells were lysed using ACK lysis buffer. The single-cell suspensions were then stimulated in complete RPMI medium containing PMA (50 ng/mL), ionomycin (1 µM), and brefeldin-A (10 µg/mL) for 4 h. After stimulation, the cells were stained with antibodies and analyzed using a BD FACSLyric Flow Cytometer. The following antibodies were used: CD45 PerCP/Cy5.5 (1:100, cat# 103132, lot# B426652, clone 30-F11, BioLegend), CD4 APC/Cy7 (1:100, cat# 100414, lot# B326190, clone GK1.5, BioLegend), CD3 FITC (1:100, cat# 100204, lot# B351638, clone 17 A2, BioLegend), and IL-17A APC (1:100, cat# 506916, lot# 358441, clone TC11-18H10.1, BioLegend). The gating strategy is shown in Supplementary Fig. 16a–c.

Histological study

Inflammation and demyelination of spinal cord were evaluated using immunofluorescence staining, Haematoxylin and Eosin staining (H&E), and Luxol Fast Blue staining (LFB), respectively. EAE mice received intravenous injections of each intervention containing 5000 U of IFNβ. At 28 days post-immunization, the spinal cords were collected, fixed in 10% (v/v) formalin for 24 h at 4 °C. For immunofluorescence staining, spinal cords were embedded in Tissue-Tek O.C.T. medium, frozen, and sectioned at 10 µm thickness. Sections were stained with Alexa fluor 647 conjugated anti-mouse CD45 (1:100, cat# 103124, lot# B364327, clone 30-F11, BioLegend). Stained sections were incubated with Hoechst 33342 and fluorescence images were obtained using a THUNDER Imaging Systems. Images analysis was conducted using the Inform 2.2.1 image analysis software (PerkinElmer). For H&E staining and LFB staining, spinal cords were embedded in paraffin blocks. Sections were incubated with hematoxylin/eosin and LFB solution, respectively. Tissue images were scanned using the Vectra Automated Multispectral Imaging System (PerkinElmer) and myelinated area was quantified using ImageJ software.

Blood biochemical analysis

From EAE mice, blood was collected 28 days post-immunization. Plasma samples were obtained by centrifugation at $2000 \times g$ for 20 min. The levels of aspartate transaminase (AST), alanine transaminase (ALT), alkaline phosphatase (ALP), creatinine, blood urea nitrogen (BUN), and total protein were evaluated using the Fuji Dri-Chem 3500 s (Fujifilm Holdings, Tokyo, Japan).

Statistical analysis

Statistical analyses were performed using GraphPad Prism 8.0. All data are presented as mean ± standard deviation (s.d.). An unpaired two-tailed Student's *t*-test was used to evaluate differences between two groups. For comparisons involving more than two groups, one-way analysis of variance (ANOVA) followed by Tukey's multiple comparisons test was conducted. A P value of <0.05 was considered statistically significant.

Reporting summary

Further information on research design is available in the Nature Portfolio Reporting Summary linked to this article.

Data availability

All datasets generated in the study are included in the manuscript, the supplementary information, and source data. Source data for all figures are provided with this paper. Source data are provided with this paper.

References

1. Ransohoff, R. M. & Engelhardt, B. The anatomical and cellular basis of immune surveillance in the central nervous system. *Nat. Rev. Immunol.* **12**, 623–635 (2012).
2. Wu, D. et al. The blood-brain barrier: structure, regulation, and drug delivery. *Signal Transduct. Target Ther.* **8**, 217 (2023).
3. Gasca-Salas, C. et al. Blood-brain barrier opening with focused ultrasound in Parkinson's disease dementia. *Nat. Commun.* **12**, 779 (2021).
4. Chu, C. et al. Hyperosmolar blood-brain barrier opening using intra-arterial injection of hyperosmotic mannitol in mice under real-time MRI guidance. *Nat. Protoc.* **17**, 76–94 (2022).
5. Terstappen, G. C., Meyer, A. H., Bell, R. D. & Zhang, W. Strategies for delivering therapeutics across the blood-brain barrier. *Nat. Rev. Drug Discov.* **20**, 362–383 (2021).
6. Fowler, M. J. et al. Intrathecal drug delivery in the era of nanomedicine. *Adv. Drug Deliv. Rev.* **165-166**, 77–95 (2020).
7. Lozano, A. M. et al. Deep brain stimulation: current challenges and future directions. *Nat. Rev. Neurol.* **15**, 148–160 (2019).
8. Bennett, C. F., Krainer, A. R. & Cleveland, D. W. Antisense oligonucleotide therapies for neurodegenerative diseases. *Annu. Rev. Neurosci.* **42**, 385–406 (2019).

9. Qu, J., Jin, J., Zhang, M. & Ng, L. G. Neutrophil diversity and plasticity: implications for organ transplantation. *Cell Mol. Immunol.* **20**, 993–1001 (2023).
10. Papayannopoulos, V. Neutrophil extracellular traps in immunity and disease. *Nat. Rev. Immunol.* **18**, 134–147 (2018).
11. Xue, J. et al. Neutrophil-mediated anticancer drug delivery for suppression of postoperative malignant glioma recurrence. *Nat. Nanotechnol.* **12**, 692–700 (2017).
12. Luo, Z. et al. Neutrophil hitchhiking for drug delivery to the bone marrow. *Nat. Nanotechnol.* **18**, 647–656 (2023).
13. Szijj, P. A., Bahou, C. & Chudasama, V. Minireview: addressing the retro-Michael instability of maleimide bioconjugates. *Drug Discov. Today Technol.* **30**, 27–34 (2018).
14. Barthelmes, J. et al. Lack of ceramide synthase 2 suppresses the development of experimental autoimmune encephalomyelitis by impairing the migratory capacity of neutrophils. *Brain Behav. Immun.* **46**, 280–292 (2015).
15. Aubé, B. et al. Neutrophils mediate blood-spinal cord barrier disruption in demyelinating neuroinflammatory diseases. *J. Immunol.* **193**, 2438–2454 (2014).
16. Walther, E. U. & Hohlfeld, R. Multiple sclerosis: side effects of interferon beta therapy and their management. *Neurology* **53**, 1622–1627 (1999).
17. Jacobs, L., O'Malley, J., Freeman, A. & Ekes, R. Intrathecal interferon reduces exacerbations of multiple sclerosis. *Science* **214**, 1026–1028 (1981).
18. Jacobs, L. et al. Multicentre double-blind study of effect of intrathecally administered natural human fibroblast interferon on exacerbations of multiple sclerosis. *Lancet* **2**, 1411–1413 (1986).
19. Kocur, M. et al. IFNβ secreted by microglia mediates clearance of myelin debris in CNS autoimmunity. *Acta Neuropathol. Commun.* **3**, 20 (2015).
20. Scheu, S. et al. Interferon β-mediated protective functions of microglia in central nervous system autoimmunity. *Int. J. Mol. Sci.* **20**, 190 (2019).
21. Boutros, T., Croze, E. & Yong, V. W. Interferon-beta is a potent promoter of nerve growth factor production by astrocytes. *J. Neurochem* **69**, 939–946 (1997).
22. Wigerblad, G. & Kaplan, M. J. Neutrophil extracellular traps in systemic autoimmune and autoinflammatory diseases. *Nat. Rev. Immunol.* **23**, 274–288 (2023).
23. Ngo, W. et al. Why nanoparticles prefer liver macrophage cell uptake in vivo. *Adv. Drug Deliv. Rev.* **185**, 114238 (2022).
24. Nauseef, W. M. Human neutrophils ≠ murine neutrophils: Does it matter? *Immunol. Rev.* **314**, 442–456 (2023).
25. Mahe, J., Meurette, A., Moreau, A., Vercel, C. & Jolliet, P. Renal thrombotic microangiopathy caused by interferon beta-1a treatment for multiple sclerosis. *Drug Des. Dev. Ther.* **7**, 723–728 (2023).
26. Gianassi, I., Allinovi, M., Caroti, L. & Cirami, L. C. Broad spectrum of interferon-related nephropathies-glomerulonephritis, systemic lupus erythematosus-like syndrome and thrombotic microangiopathy: a case report and review of literature. *World J. Nephrol.* **8**, 109–117 (2019).
27. Warnatsch, A., Ioannou, M., Wang, Q. & Papayannopoulos, V. Inflammation. Neutrophil extracellular traps license macrophages for cytokine production in atherosclerosis. *Science* **349**, 316–320 (2015).
28. Wilson, A. S. et al. Neutrophil extracellular traps and their histones promote Th17 cell differentiation directly via TLR2. *Nat. Commun.* **13**, 528 (2022).
29. Swamydas, M., Lionakis, M. S. Isolation, purification and labeling of mouse bone marrow neutrophils for functional studies and adoptive transfer experiments. *J. Vis. Exp.* **10**, e50586 (2013).
30. Stromnes, I. M. & Goverman, J. M. Active induction of experimental allergic encephalomyelitis. *Nat. Protoc.* **1**, 1810–1819 (2006).
31. Lee, H. G. et al. Disease-associated astrocyte epigenetic memory promotes CNS pathology. *Nature* **627**, 865–872 (2024).
32. Zuo, Y. et al. Autoantibodies stabilize neutrophil extracellular traps in COVID-19. *JCI Insight* **6**, e150111 (2021).

Acknowledgements

This research was funded by grants from the National Research Foundation (NRF) of Korea, Ministry of Science and ICT, Republic of Korea (NRF-2018R1A5A2024425, J.L.), from the Alchemist Project of the Korea Evaluation Institute of Industrial Technology (KEIT 20018560, NTIS 1415184668, J.L.), the Ministry of Trade, Industry & Energy, Republic of Korea, and from Ascending SNU Future Leader Fellowship through Seoul National University (0430-20240011, Y.W.), Republic of Korea.

Author contributions

Y.W., J.P., and J.L. were responsible for most of the investigations, methodology development, data collection/analysis, and writing the manuscript. Q.V.L., J.B., J.C., and E.X. assisted with the in vivo experiments. J.L. was responsible for the funding and resources acquisition, supervising the project. Y.K.O. was responsible for resources acquisition, supervising the project, revising, and editing the manuscript.

Competing interests

The authors declare no competing interests.

Additional information

Supplementary information The online version contains supplementary material available at https://doi.org/10.1038/s41467-024-54817-7.

Correspondence and requests for materials should be addressed to Jaiwoo Lee or Yu-Kyoung Oh.

Peer review information *Nature Communications* thanks Qiang Liu, and the other, anonymous, reviewer(s) for their contribution to the peer review of this work. A peer review file is available.